

THE *SPITZER* c2d SURVEY OF LARGE, NEARBY, INSTERSTELLAR CLOUDS. II. SERPENS OBSERVED WITH IRAC

PAUL M. HARVEY,¹ NICHOLAS CHAPMAN,² SHIH-PING LAI,² NEAL J. EVANS, II,¹ LORI E. ALLEN,³ JES K. JØRGENSEN,³
LEE G. MUNDY,² TRACY L. HUARD,³ ALICIA PORRAS,³ LUCAS CIEZA,¹ PHILIP C. MYERS,³ BRUNO MERÍN,⁴
EWINE F. VAN DISHOECK,⁴ KAISA E. YOUNG,¹ WILLIAM SPIESMAN,¹ GEOFFREY A. BLAKE,⁵ DAVID W. KOERNER,⁶
DEBORAH L. PADGETT,⁷ ANNEILA I. SARGENT,⁸ AND KARL R. STAPELFELDT⁹

Received 2005 November 23; accepted 2006 February 7

ABSTRACT

We present maps of 0.89 deg^2 of the Serpens dark cloud at 3.6, 4.5, 5.8, and $8.0 \mu\text{m}$ observed with the *Spitzer Space Telescope* Infrared Array Camera (IRAC). We discuss in detail the data processing carried out by the c2d team on IRAC data. More than 100,000 compact sources have been extracted, but we confine most of our discussion to the most reliable subset of these sources. This includes those that are detected above 7σ in all four IRAC bands or those detected in the two shorter IRAC bands together with 2MASS. We estimate completeness limits for our survey from Monte Carlo tests with artificial sources inserted into the *Spitzer* maps. We compare source counts, colors, and magnitudes in the Serpens cloud to two reference data sets, a 0.10 deg^2 set of low-extinction regions near the dark cloud and a 1 deg^2 subset of the SWIRE Elais N1 data that was processed through our pipeline. We find that it is possible to identify more than 200 young stellar object (YSO) candidates from color-magnitude and color-color diagrams, most of which were previously unknown. In addition to the dense area of new star formation known before in the “core” region (cluster A), we also find a moderately rich area to the south (cluster B). Our mapped area also includes the Herbig Ae star VV Ser, whose *Spitzer* images have been carefully modeled in a separate study. The extreme sensitivity of *Spitzer* IRAC allows us to search to very low luminosity limits for young substellar objects. The comparison of the Serpens region with the reference areas suggests that a population of infrared excess sources exists in Serpens at least down to luminosities of $L \sim 10^{-3} L_\odot$ and possibly lower.

Subject headings: infrared: ISM — ISM: clouds

1. INTRODUCTION

The *Spitzer* Legacy project “From Molecular Cores to Planet-forming Disks” (c2d; Evans et al. 2003) selected five nearby star-forming regions to map, including Serpens. These clouds were chosen because they are nearby, allowing *Spitzer*’s modest angular resolution to be well matched to typical stellar densities and providing a detection limit sufficiently low to permit complete sampling of the young stellar population down to substellar luminosities and masses. The Serpens molecular cloud covers more than 10 deg^2 as mapped by optical extinction measurements (Cambrésy 1999). The c2d program has mapped a 0.89 deg^2 portion of this cloud that includes a very well studied cluster of infrared and submillimeter sources (Eiroa & Casali 1992;

Hogerheijde et al. 1999; Hurt & Barsony 1996; Harvey et al. 1984; Testi & Sargent 1998). At its distance of $260 \pm 10 \text{ pc}$ (Straizys et al. 1996) this corresponds to an area of about $2.5 \times 9 \text{ pc}$. The cloud was identified as one in which a relatively high level of clustered star formation appears to be occurring (e.g., Testi et al. 2000). The initial goal of this project is to identify the population of young stellar and substellar objects in the Serpens cloud and determine the relationship between these objects, their locations in the cloud relative to the cloud properties, and their evolutionary state.

We report here on the observations made with *Spitzer*’s Infrared Array Camera (IRAC) of the c2d portion of the Serpens cloud. This area includes the well-studied IR/submillimeter cluster in the region generally called the “core” (referred to as cluster A in this paper) that was included in observations by the *Spitzer* guaranteed time observations (GTO) program, as well as an area to the south with known pre-main-sequence stars as evidenced by optical spectra, several low-luminosity T Tauri-like stars from the Herbig and Bell catalog (Herbig & Bell 1988), and the well-studied Herbig Ae-Be star VV Ser (Berrilli et al. 1992; Blake & Boogert 2004; Chavarría-K. 1988; Li et al. 1994; Hillenbrand et al. 1992; K. M. Pontoppidan et al. 2006a, in preparation; 2006b, in preparation). Much of the c2d area has also been observed by previous infrared space missions, including the *Infrared Astronomical Satellite* (IRAS; Zhang et al. 1988b) and to a lesser extent the *Infrared Space Observatory* (ISO; Kaas et al. 2004). Our IRAC observations provide the most sensitive and highest spatial resolution search yet for young low-mass objects in this star-forming cloud and for faint circumstellar emission from relatively small amounts of dust. The limiting sensitivity is a factor of 100 below that of ISO at comparable wavelengths, for example.

¹ Astronomy Department, University of Texas at Austin, 1 University Station C1400, Austin, TX 78712-0259; pmh@astro.as.utexas.edu, nje@astro.as.utexas.edu, lcieza@astro.as.utexas.edu, kaisa@astro.as.utexas.edu, spies@astro.as.utexas.edu.

² Astronomy Department, University of Maryland, College Park, MD 20742; chapman@astro.umd.edu, slai@astro.umd.edu, lgm@astro.umd.edu.

³ Smithsonian Astrophysical Observatory, 60 Garden Street, MS42, Cambridge, MA 02138; leallen@cfa.harvard.edu, jjorgensen@cfa.harvard.edu, thuard@cfa.harvard.edu, aporras@cfa.harvard.edu, pmyers@cfa.harvard.edu.

⁴ Leiden Observatory, Postbus 9513, 2300 RA Leiden, Netherlands; merin@strw.leidenuniv.nl, ewin@strw.leidenuniv.nl.

⁵ Division of Geological and Planetary Sciences, MS 150-21, California Institute of Technology, Pasadena, CA 91125; gab@gps.caltech.edu.

⁶ Northern Arizona University, Department of Physics and Astronomy, Box 6010, Flagstaff, AZ 86011-6010; koerner@physics.nau.edu.

⁷ Spitzer Science Center, MC 220-6, Pasadena, CA 91125; dlp@ipac.caltech.edu.

⁸ Division of Physics, Mathematics, and Astronomy, MS 105-24, California Institute of Technology, Pasadena, CA 91125; afs@astro.caltech.edu.

⁹ Jet Propulsion Laboratory, MS 183-900, California Institute of Technology, 4800 Oak Grove Drive, Pasadena, CA 91109; krs@exoplanet.jpl.nasa.gov.

TABLE 1
OBSERVATIONS SUMMARY

AOR Key	Date (2004)	Program/Program ID
On-Cloud Observations		
0003652352.....	Apr 1	IRAC GTO/6
0005710592.....	Apr 4	c2d/174
0005710848.....	Apr 5	c2d/174
0005711104.....	Apr 5	c2d/174
0005711360.....	Apr 5	c2d/174
0005711616.....	Apr 5	c2d/174
0005711872.....	Apr 5	c2d/174
0005712384.....	Apr 5	c2d/174
0005712640.....	Apr 5	c2d/174
0005712896.....	Apr 5	c2d/174
0005713152.....	Apr 5	c2d/174
Off-Cloud Observations		
0005714432.....	Apr 5	c2d/174 (1)
0005714668.....	Apr 5	c2d/174 (2)
0005714944.....	Apr 5	c2d/174 (3)
0005715200.....	Apr 5	c2d/174 (4)
0005715456.....	Apr 5	c2d/174 (5)
0005715712.....	Apr 5	c2d/174 (6)
0005715968.....	Apr 5	c2d/174 (7)
0005716244.....	Apr 5	c2d/174 (8)

2. OBSERVATIONS

The area chosen for mapping was defined by the $A_V > 6$ contour in the extinction map of Cambrésy (1999) and by practical time constraints (Evans et al. 2003). The entire cloud was observed twice with *Spitzer*'s IRAC camera in 2004 April (Table 1). For the area covered by the c2d observing only, the first observation, or epoch, was separated from the second by about 6 hr. The area covered by the IRAC GTO team was observed once by them (Winston et al. 2005) and at a second epoch several days later with c2d observations. This separation of observation epochs was designed to enable the detection and removal of asteroids, which will be brightest at 8 μm . With the combination of our c2d observations and the recently released *Spitzer* GTO observations of Serpens (Winston et al. 2005), all areas were observed with at least one short integration in “high dynamic range” mode (HDR) of 0.4 s and four integrations of 10.4 s (2 epochs/2 dithers). The ecliptic latitude of this area, $\sim +23^\circ 5'$, is high enough that asteroids are expected to be rare. Indeed, in our examination of the images made from individual epochs we found no examples of obvious asteroids. In other c2d clouds closer to the ecliptic, the typical asteroid motion observed between epochs was between 10'' and 1'.

In addition to this area of the Serpens cloud defined by relatively high A_V , we also observed eight small regions (off-cloud) around the molecular cloud with relatively low A_V in order to determine the background star counts (Table 1). Figure 1 shows the on- and off-cloud regions superimposed on the Cambrésy (1999)

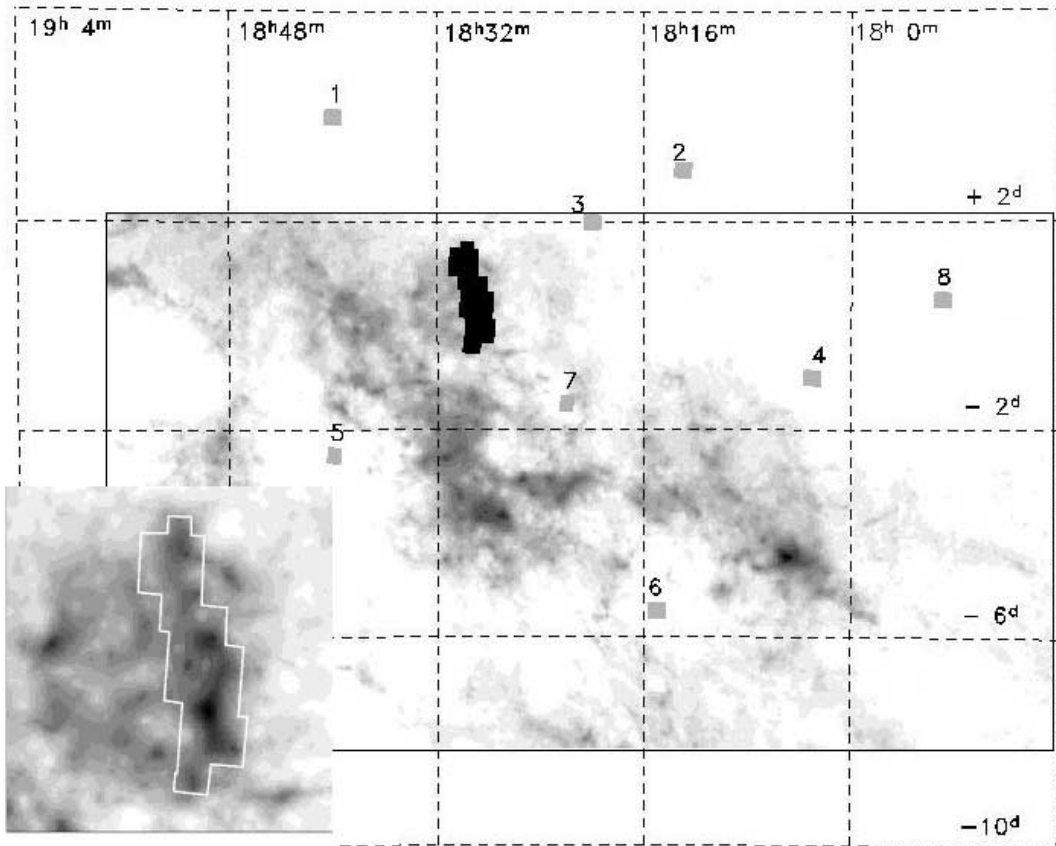


FIG. 1.—Map showing main Serpens cloud region observed, as well as the eight off-cloud regions (marked by their numerical designations) in areas of low extinction. The gray-scale image shows the extinction mapped by Cambrésy (1999). The inset shows an enlargement of the on-cloud area mapped in the Serpens cloud.

extinction map of the cloud. These regions were selected to provide a range of Galactic latitudes and longitudes around the position of the main map. The two regions, Nos. 1 and 6, whose latitudes, $+04^{\circ}25'$ and $+05^{\circ}30'$, straddle most closely that of the main map (with Galactic latitude ranging from $+04^{\circ}40'$ to $+05^{\circ}40'$) have star count distributions virtually identical to those observed in the low-extinction parts of the Serpens cloud. Therefore, we have used the sum of these two areas only in further comparison of the On and Off cloud areas. The total area of these two regions is 0.16 deg^2 , but the total area of overlap for all four IRAC bands is only about 0.1 deg^2 , or about $\frac{1}{9}$ of the total area mapped within the Serpens cloud.

3. DATA REDUCTION

The IRAC images were processed by the Spitzer Science Center (SSC) using a standard pipeline to produce basic calibrated data (BCD) images. The pipeline used was version S11. These BCD images were then processed by the c2d pipeline version 2005/May, which we describe in brief below. A detailed description of this processing is included in the documentation for the second delivery of c2d data to the SSC (Evans et al. 2005).

3.1. Image Problems and Corrections

The SSC pipeline produces BCD images that have subtracted the dark and bias levels from the raw data, followed by flat-fielding and sky subtraction. In the BCD images, any instrumental signatures, bad pixels (those with atypical sensitivities), and pixels saturated by very bright sources have been identified within mask files. Overall flux calibration, expressed in physical units of MJy sr^{-1} , is estimated by the SSC to be accurate to within 10%. We discuss below the estimated absolute uncertainty in extracted source fluxes.

With each astronomical observation request (AOR), the SSC releases two mask files (`pmask` and `dmask`) that identify most pixels affected by various peculiarities. The purpose of the `pmask` is to identify pixels that are permanently damaged, that exhibit dark currents or sensitivities that are consistently either too variable or extreme to be reliable. The purpose of the `dmask`, on the other hand, is to identify pixels that are affected by various peculiarities, some of which do not render a pixel nonusable or “bad.” One `pmask` is sufficient for each band in an AOR, while a `dmask` is released for each IRAC BCD image.

We combine the information in the SSC mask files together with additional checks to create a new “`c2dmask`” file for each BCD image that masks all pixels believed to be bad at this time. All pixels with any bits set in the `pmask` are considered bad pixels and indicated as such in the `c2dmask`. In addition, pixels with either of bits 5 or 8–14 set in the `dmask` are also considered bad pixels by the `c2dmask`. Finally, we examine each BCD image to identify bad pixels not included within the `pmask` or `dmask`. If a pixel has a value greater than 20σ times the mean of the surrounding pixel values, then it is considered a bad pixel by the `c2dmask`. This criterion is effective for identifying isolated, grossly bad pixels not identified by the `dmask`s or `pmask`s while not falsely identifying pixels near the peaks of stellar point-spread functions (PSFs) as bad pixels. This method is not effective for automatically identifying streaks of bad pixels, which are due to inclined cosmic-ray hits.

Three artifacts occurring near moderately bright sources, muxbleed, pulldown, and banding features, are corrected to the extent possible in our image processing. Muxbleed occurs in the rows on which these sources are positioned in band 1 and band 2

images; banding occurs in the rows in band 3 and band 4 images. Pulldown, primarily seen in band 1 and band 2 images, occurs in the columns containing moderately bright sources and is corrected in all IRAC bands. In addition, we correct for the “first-frame effect” as described below.

We use an IDL procedure provided by D. Stern (JPL and GOODS Legacy Team) to detect and correct pixels affected by muxbleed. This procedure is very reliable in detecting these pixels, but improvements to the corrections are currently underway by Stern and the SSC. The muxbleed corrections, when relatively small, are reliable, while larger muxbleed corrections are not as ideal. Nevertheless, in either case, they represent improvements in the image quality and therefore are applied.

The muxbleed-correcting procedure searches for pixel values greater than 10,000 DN, which arise from either moderately bright sources or cosmic-ray hits. Such pixels are known to be the source of muxbleed. Muxbleed pixels caused by a pixel with value between 10,000 and 30,000 DN are corrected by interpolation of a table of predetermined corrections as a function of distance from the muxbleed source. Muxbleed arising from pixels with values greater than 30,000 DN is corrected by fitting an empirically derived function to the muxbleed pixel values. The muxbleed corrector was written specifically for IRAC band 1 images, but we also apply these corrections to band 2 images. Visual inspection of these images suggests that these corrections can be applied to the band 2 images as well.

To correct for column pulldown and banding effects, we use two IDL procedures provided by R. Gutermuth (Smithsonian Astrophysical Observatory). The procedure for column pulldown is a somewhat revised version of a procedure previously provided by SSC. Comparison of the results of running the pulldown-correcting procedure used in our pipeline with those from the current SSC pulldown-correcting procedure demonstrates that the resulting corrections do not differ significantly between the two procedures. These procedures are very reliable in both detecting and correcting columns affected by pulldown. On the other hand, detection and correction of banding is often not as ideal. Even so, the banding corrections applied to our images are never overcorrections and still represent improvements in the image quality.

The corrections for pulldown are additive constants applied to the affected columns of an image. After masking bad pixels, the median pixel value of each column is computed. The ensemble of these median values form a projected median-valued row, which is compared with a smoothed version of this projected row to identify columns with discrepant median pixel values, presumably due to the column pulldown effect. The pixel values in the deviant columns are then shifted to match the median of the smoothed projected median-valued row. This algorithm searches for deviant columns rather than the moderately bright sources that cause column pulldown; thus, it is possible that the algorithm could automatically apply inappropriate pulldown corrections to columns on which no moderately bright sources are positioned. However, the parameter values involved in the algorithm have been optimized and tested such that very rarely, if ever, are columns corrected that are not affected by pulldown. A similar algorithm is employed to detect and correct rows affected by banding in Bands 3 and 4.

Finally, the data delivered are corrected for the first-frame effect. The bias level of a raw image depends on the elapsed time between obtaining the image and the previous observation. These bias levels have been properly removed during the SSC pipeline to reduce raw images to BCD images, with the exception of the first long-exposure image (i.e., 12 or 30 s image, in our case) of

band 3. To facilitate our correcting of the first-frame effect in the first long-exposure, band 3 image in our observations, the first band 3 image obtained in each AOR is a short-exposure (i.e., 0.6 s) image. In this way, the elapsed time between the first long-exposure, band 3 image and the previous image is the same in all our AORs. Thus, these BCD images themselves can be used to correctly subtract the residual bias remaining in these images after the SSC pipeline.

Our procedure for correcting the first-frame effect in IRAC observations of a particular molecular cloud involves constructing a “bias correction image.” We begin constructing this bias correction image by collecting all the first long-exposure band 3 images from the set of AORs for that molecular cloud. For each of these images, the median pixel value in the image is subtracted from all the pixels. Then, a median-filter stack of these images, followed by a subtraction of the median pixel value, results in the bias correction image. After correcting for any banding or column pulldown artifacts in the original band 3 BCD images, the bias correction image is subtracted from the first of these long-exposure images in each AOR.

Currently, we do not mask stray light that appears in some of the IRAC images. This stray light originates from bright sources just outside the field of view and scatters onto the detector.

3.2. Mosaicking and Source Extraction

The mosaicking and source extraction processing steps are closely linked in the c2d analysis of IRAC data. This is because we use a preliminary source extraction on the short integration sample from the HDR (0.4 s exposure) data set to mask out likely saturated areas in the longer integration frames for the mosaicking (and final source extraction) steps. A complete description of these processing steps is given by P. M. Harvey et al. (2006, in preparation), but we summarize the important features here.

All our mosaics are produced using the SSC’s “Mopex” software suite (Makovoz & Marleau 2005). This is comprised of a number of modules that are typically used sequentially from Perl scripts. For our IRAC data we use the position refinement module to determine the best positional match between overlapping frames and the overlap module to determine the best common background value at points of overlap between frames (because the precise background level in IRAC frames is uncertain due to the lack of contemporaneous dark frames and inoperability of the IRAC shutter). We also use all the outlier detection modules, together with the natural redundancy in our data set, to mask out all but the faintest radiation hits. In the final two-epoch mosaic, this processing masks out at least 95% of the asteroids in the mosaic. The mosaics are produced with a 1:1 pixel ratio relative to the input BCD frames.

After production of a mosaic of all the 0.4 s frames with pointing refinement, overlap correction, and outlier detection applied, we extract the brighter sources. We then use their positions and brightnesses to determine which additional pixels to mask in the longer integration frames from both epochs. This extraction list is also available for comparison with that from the full, all-frame mosaic, as a check on any residual saturation effects. We next produce four additional mosaics: (1) the long-integration frames from both epochs together, (2) the combination of all frames from both epochs including the 0.6 s frames (this is used for the final flux determination of reliable sources), and (3) mosaics for each of the two individual epochs with the 0.6 s frames from the first epoch included with each (these are used both to estimate extracted source reliability and to search for transient sources, typically asteroids). Source extraction is applied to all of these mosaics.

Our source extraction tool, c2dphot, is based on the venerable “DoPHOT” code described by Schechter et al. (1993). Our version includes the following important modifications to DoPHOT: it (1) utilizes a digitized point-source profile rather than analytic to best match the real *Spitzer* data; (2) accepts floating point input FITS images and computes output fluxes based on the *Spitzer* surface brightness units in the BCD-level images; (3) accepts input masks to avoid using pixels that have been declared bad for whatever reason; and (4) includes a multiframe mode, c2dphot_m, that fits fluxes and positions using the entire stack of individual BCD frames that include the input source position, using the unsmoothed instrumental PSF rather than that produced by the mosaicking process. The most significant unchanged aspect of c2dphot/DoPHOT is the basic source extraction process. In particular, c2dphot starts at an upper flux level, finds and characterizes sources above that level, and subtracts them from the image. It then works its way down in flux, typically with a factor of 2 step each time, doing the same thing until it reaches the lower flux limit input by the user. This obviously implies that the lower limit to objects detected is set by the brightest pixel in the object’s image relative to the local background. For all the data presented here, we began by setting this threshold such that the faintest objects typically had a signal-to-noise ratio S/N $\sim 6\text{--}8$. If c2dphot finds an object that is better fit by a two-axis ellipsoid than the numerical point-source profile, it will classify the object as extended (type 2) and produce estimates of the source size and tilt of the ellipse using DoPHOT’s algorithms.

As in any source extractor, there are many tunable parameters in c2dphot_(m) to enable it to deal with a variety of problems or characteristics in the data. The most sensitive parameters for both accurate source extraction and photometry are the sizes of the search box, fitting box, and aperture photometry boxes. For these data we used search and aperture boxes of typically 7 pixels and a fitting box of 9 pixels, based on a number of tests on simulated data sets, as well as a variety of real data from *Spitzer*. Other tunable parameters include thresholds for deciding whether a source is extended, whether an initial detection is better fit by a tilted plane, and whether a source is so small that it is more likely to be a previously undetected radiation hit. These have all been tuned to levels that appear appropriate from careful visual inspections of subsets of the data.

The final source extraction list is produced in a two-step process, first running c2dphot on the relevant mosaic and then using the extraction list from that step as an input to c2dphot_m to refine the positions and fluxes of the sources that are found from the mosaic with its higher S/N. As mentioned above, this ensures that the source characteristics are derived from the least-processed form of the data, the BCD-level products, although we retain the source “image type,” extended versus pointlike, derived from the mosaic extraction.

The calibration of source fluxes is done by using the aperture fluxes found by c2dphot_(m) to scale the fluxes that result from the model fitting to object profiles. Otherwise, small errors in the assumed PSF could lead to unacceptably large errors in the derived fluxes (that are essentially a product of peak flux density multiplied by effective PSF area).

Flux and position uncertainties in c2dphot_(m) are calculated in a standard way from a numerical estimate of the Hessian matrix (Press et al. 1992; Sivia 1996). In particular, the matrix of partial gradients of χ^2 is calculated numerically for variations in the four model parameters (for point sources). This is done by fixing each parameter at levels offset slightly above and below the best-fit parameter and calculating the change in χ^2 for all

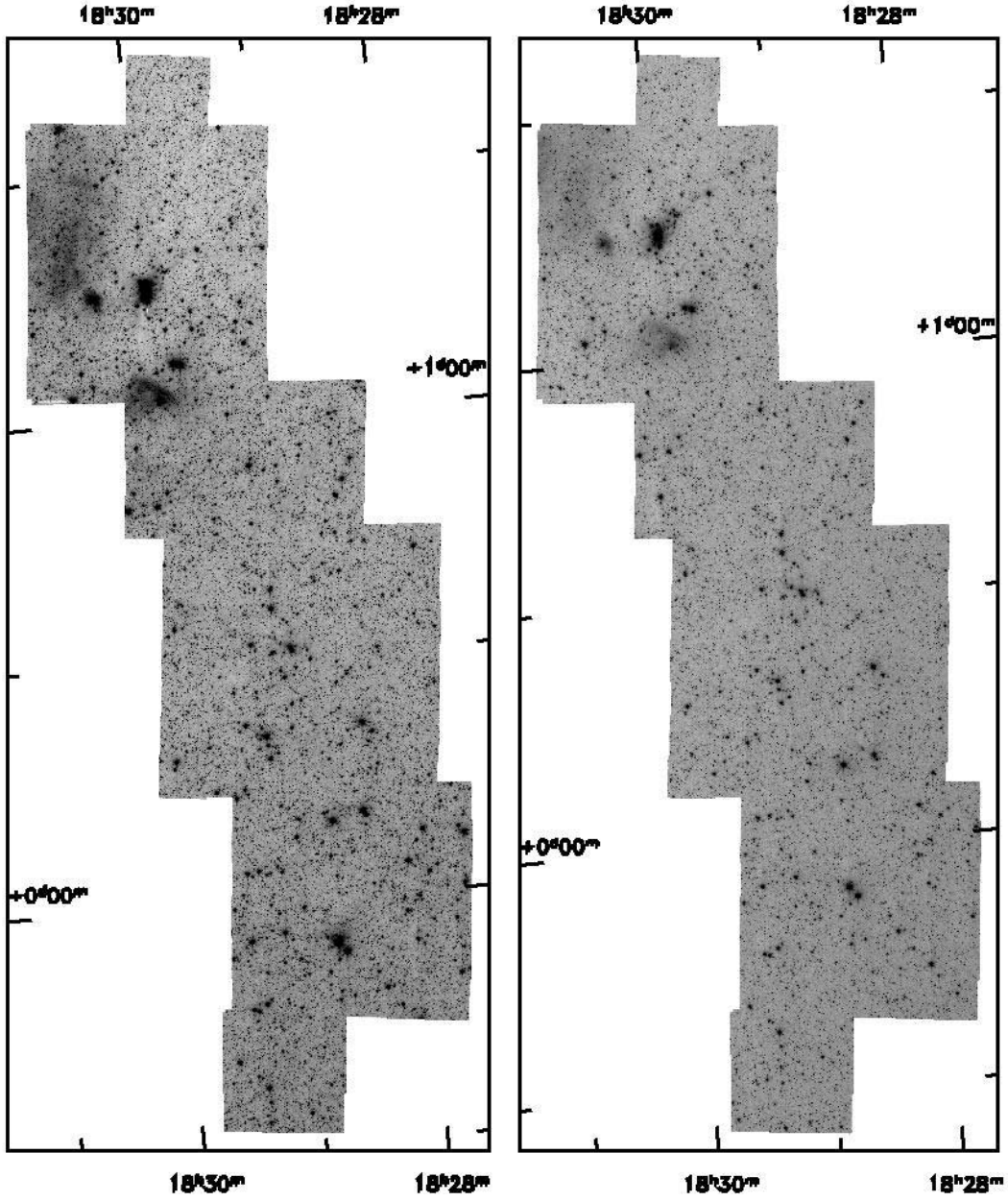


FIG. 2.—Image mosaics for IRAC band 1 ($3.6 \mu\text{m}$; left) and band 2 ($4.5 \mu\text{m}$; right). Note that the coverage for bands 2 and 4 differs from that of bands 1 and 3 because of their offset in the focal plane of *Spitzer*.

combinations of offset parameters. The inverse of this matrix then gives an error estimate, at least in the case in which the errors are reasonably behaved. For extended (type 2) extractions a similar procedure is part of DoPHOT and c2dphot(m) using analytic rather than numerical estimates of the derivatives.

Figures 2 and 3 show the final mosaic images for all four IRAC bands individually. Figure 4 shows a color mosaic using IRAC bands 1, 2, and 4 of the entire mapped area that has four-band data. Several interesting regions are magnified in the insert images and discussed below. We also discuss the diffuse emission in Figure 4 in §§ 8.3 and 8.4.

4. DATA QUALITY

4.1. Image Quality

There are a number of small instrumental effects that appear in the final mosaic images that are difficult to remove completely,

some of which also affect the source extraction process. As described earlier in § 3.1, detector problems like muxbleed, column pulldown, and banding can only be partially corrected at this time, since they are nonlinear effects that are only partially understood. Most of the false source extractions due to these defects have been removed by hand from the final high-quality catalog. Defects in the images due to stray light are most commonly diffuse and also relatively uncommon, so they have had little or no effect on the compact sources identified in the data. Two other point or compact source problems almost certainly still exist at a low level in the data: weak cosmic-ray hits and faint asteroids. Since the “outlier detection” modules in Mopex use S/N thresholds to find outliers, objects whose brightness is not strongly divergent from the background plus typical noise will not be filtered out. We therefore expect a modest number of such interlopers in our data. Filtering at a relatively high signal level, e.g., 7σ , is expected to eliminate most of these objects. In § 5 we

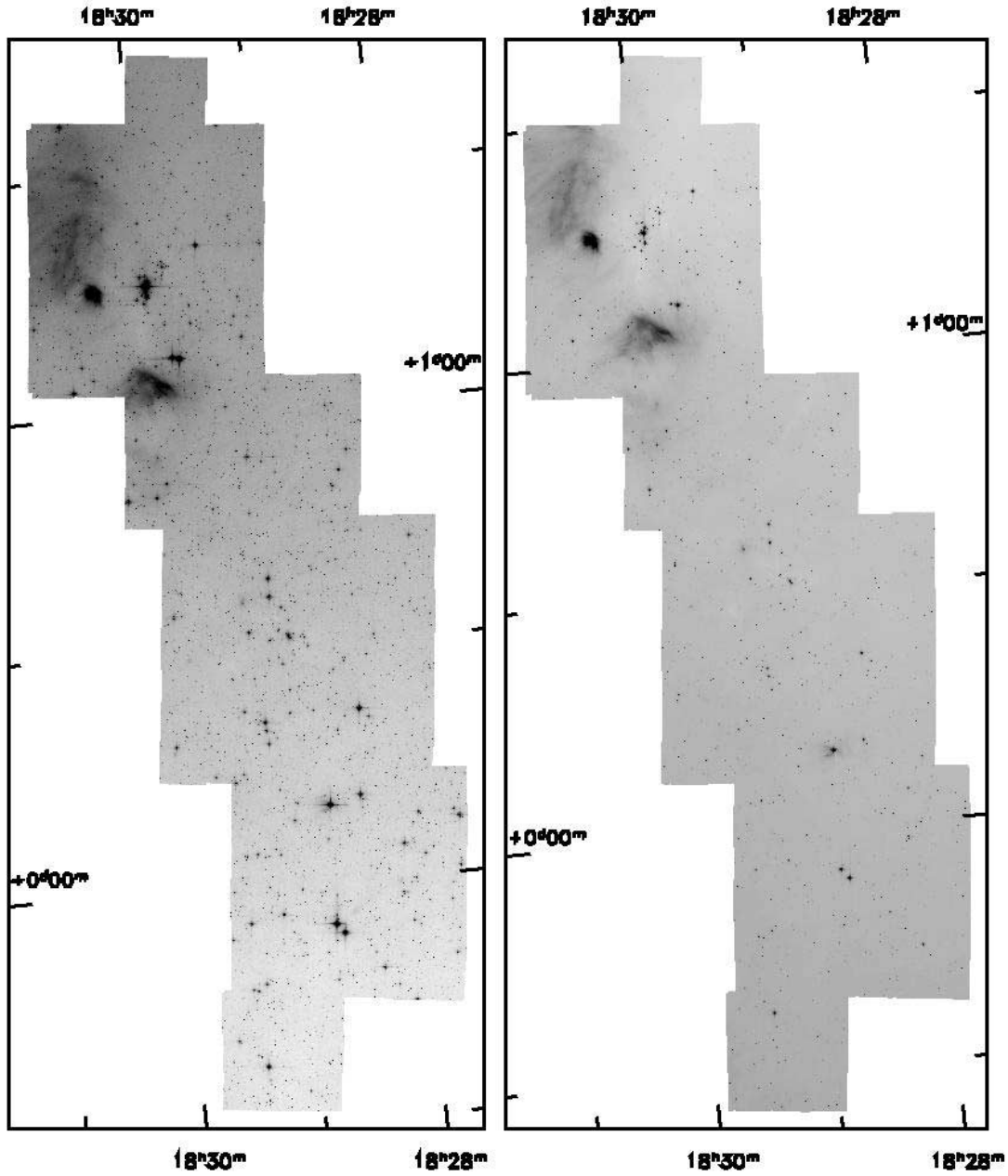


FIG. 3.—Image mosaics for IRAC band 3 ($5.8 \mu\text{m}$; left) and band 4 ($8.0 \mu\text{m}$; right).

also discuss further catalog processing that makes use of multiband detections to improve the reliability. Most faint radiation hits and asteroids are filtered out in this stage of processing.

4.2. Completeness and Reliability

We have estimated the completeness level and reliability of the source extractions by one commonly used Monte Carlo technique, inserting artificial “stars” into the images and then reprocessing those images and measuring what fraction of the artificial objects were found and how accurately their fluxes were determined. For each mosaic image in the four IRAC bands we inserted 2500 sources, 100 in each of 25 mag bins, separated in bins of 0.25 mag. Table 2 lists the range of magnitudes and corresponding fluxes for each band. The artificial source profiles were generated using the PSF that we use for the source extractions, which is close to but obviously not identical to the actual PSF. The sources were inserted at random positions over the area of each mosaic that was

farther than 2 pixels from any edge of the valid mosaic. Then the single-frame version of c2dphot was used to extract all sources in the mosaic. In addition to this mosaic/extraction, we also produced an artificial-star-only mosaic with exactly the same stars/positions and a noise level as close as possible to that in the original image, based on the lower 50 percentile of pixels in the original mosaic image. Comparison of the extraction statistics from this latter image with that in the former gives an estimate of what fraction of incompleteness is due to source confusion versus a simple lack of S/N.

Figure 5 shows the results of the comparison of the extraction list and the truth list for both the true+artificial image and the artificial-star-only image. The fact that in most cases it is impossible to see the difference between the “unreliable” line and zero shows that an insignificant number of false detections are found except at the very lowest flux levels in some of the bands. The fact that the “completeness” ratio is essentially unity for

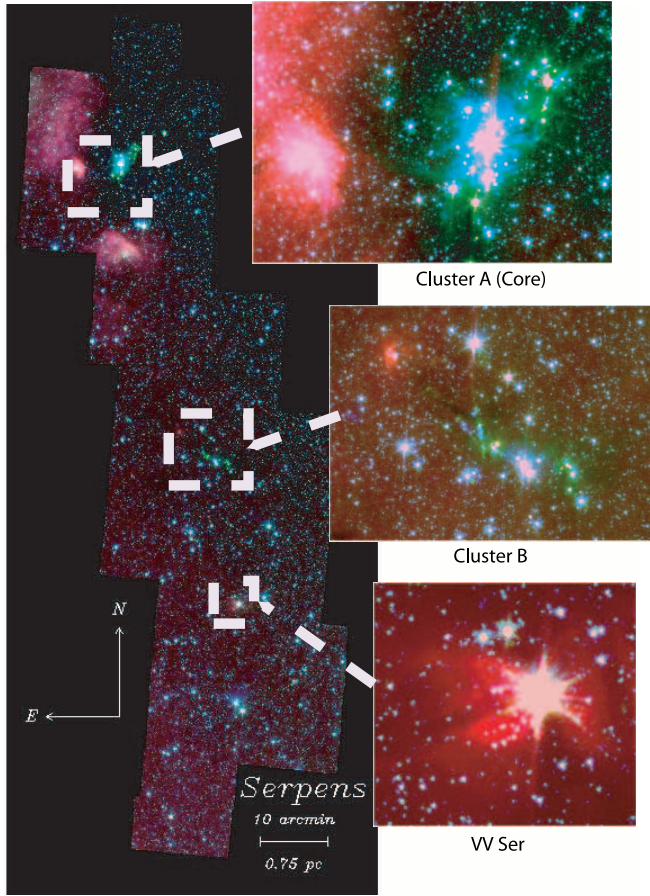


Fig. 4.—Color image made from IRAC1 (blue), IRAC2 (green), and IRAC4 (red) images, for the area observed in common in all four IRAC bands. Several of the more interesting objects/areas are shown at higher magnification in the inset images.

many of the examples for the artificial-star-only image shows that by far most of the incompleteness for the real+artificial-star image is due to the high density of stars in the Serpens region leading to substantial confusion/image overlap. In fact, we have examined several tens of “missing” stars in the real+artificial image to determine what sorts of problems led to their not being extracted. In *every* case we checked, the unextracted star was invisible to our hands-on check due to being obscured by a real star in the image that was brighter enough to mask the undetected artificial star. In regions of substantial source confusion, e.g., the Galactic plane observed with IRAC, it is clear that the precise definition of “completeness limit” depends on what astrophysical question is being considered.

Figures 6 and 7 illustrate the errors in extracted magnitudes in both total numbers at different error levels and typical error as a function of magnitude. Figure 8 shows the differential number

counts for sources in each band as a function of magnitude along with the counts for the sum of the two closest “off-cloud” reference regions (OC1 and OC6) and the predicted star counts using a C-version of the Wainscoat et al. (1992) model provided by J. Carpenter (2001, private communication). These plots provide another estimate of completeness limits by illustrating the turnover in source counts both in an absolute sense and in comparison to the expected background star density, which dominates at these low Galactic latitudes.

The absolute calibration uncertainties are not included in our uncertainties. They are described in the data handbooks for the instruments but may be updated with time. With the level of processing applied to our data we believe these are better than 15% for IRAC for point sources.

5. HIGH-RELIABILITY BANDMERGED CATALOG

The final stage of data processing prior to science analysis of c2d images involves the creation of bandmerged catalogs. The process is described below. The chief difference between the method employed here and that described in Evans et al. (2005) is that *no* explicit flux cutoff is imposed on the catalog created for this paper. Instead we have used S/N criteria described below to sort out the most reliable objects.

For each band, the three source extraction lists (epoch1, epoch2, and combined epochs) were checked for “self-matches” within an epoch; two sources extracted within one epoch but with positional matches of $\leq 2.0''$ were considered to be the same source. The fluxes of the detections were summed, and the position of the source was calculated as the weighted mean. The three lists were also merged together to cross-identify sources with positional matches of $2.0''$ or less. The epoch-merged source lists for each band were visually inspected to remove diffraction spikes, column pull-down, latent images, and other image artifacts that were misidentified as sources.

The epoch-merged source lists for each band were then merged as follows. First, detections in each IRAC band were identified with a single source if the differences in central positions were $\leq 2.0''$. This bandmerged IRAC catalog was then merged with the $24\ \mu\text{m}$ MIPS1 band using a larger distance, $4.0''$. The larger distance was used because of the larger PSF at $24\ \mu\text{m}$ compared to IRAC. Last, the IRAC+MIPS catalog was compared with the Two Micron All Sky Survey (2MASS) catalog using a position-matching criterion of $2.0''$. In cases with multiple 2MASS or *Spitzer* sources within $2.0''$, the closest match between 2MASS and *Spitzer* was kept. When a 2MASS source did not have a *Spitzer* source, the 2MASS source was added to the catalog.

5.1. Reliability Criteria

The final catalog produced by the above processing results in a very large number of “sources,” most of which are near the flux limit of our survey. In order to perform preliminary statistical studies of the catalog in a reasonably reliable way, we have substantially trimmed the complete catalog in several ways.

TABLE 2
MAGNITUDE RANGES FOR ARTIFICIAL STARS USED FOR COMPLETENESS TESTS

Band	Faint Magnitude (mag)	Minimum Flux (mJy)	Bright Magnitude (mag)	Maximum Flux (mJy)
IRAC 1.....	17.42	0.03	11.42	7.54
IRAC 2.....	16.94	0.03	10.94	7.54
IRAC 3.....	15.41	0.08	9.41	20.1
IRAC 4.....	14.50	0.10	8.50	25.1

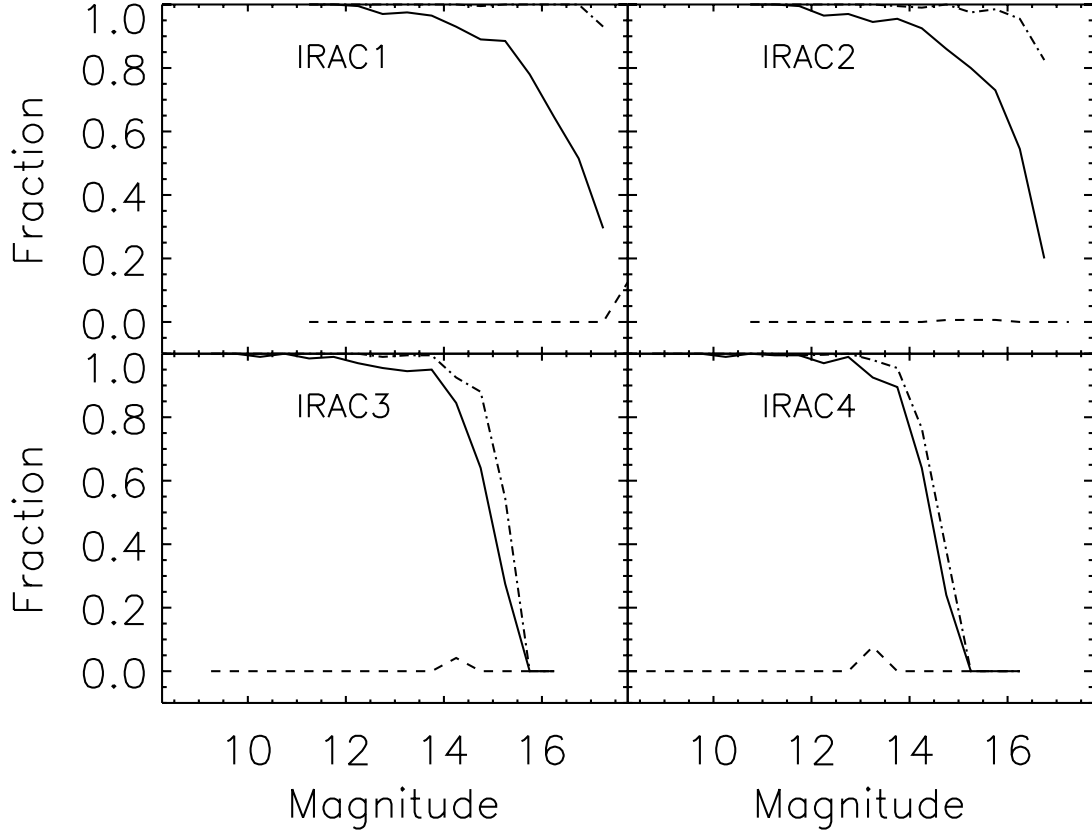


FIG. 5.—Completeness/reliability plots for extractions of artificial stars from the Serpens cloud mosaic for the four IRAC bands. In each panel the upper solid curve shows the completeness level for artificial sources as a function of magnitude. The dash-dotted curve shows the completeness level for extractions from a mosaic of only artificial stars with no Serpens background sources, but with the same noise level as in the real image. The difference between these curves illustrates the effect of source confusion on the completeness level. The lower dashed curve (mostly equal to zero) shows the fraction of sources extracted from the artificial-star-only image that were false detections (e.g., noise spikes).

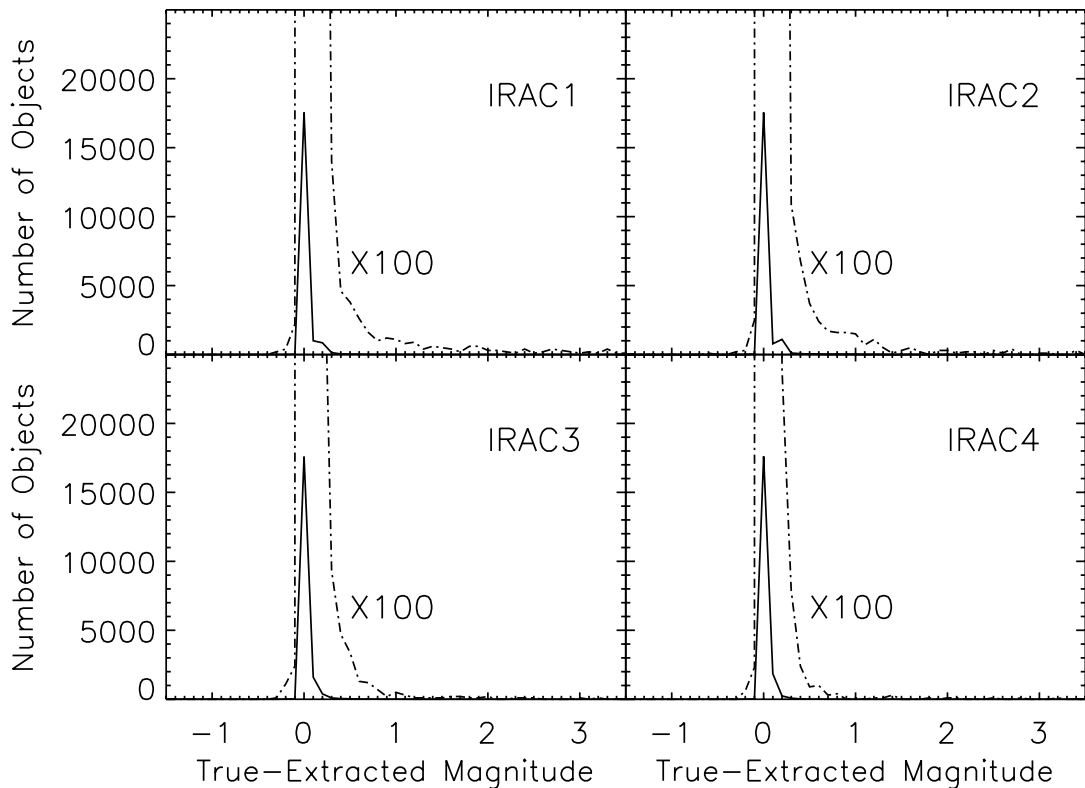


FIG. 6.—Histogram of differences between true vs. extracted magnitude for the extractions of artificial stars inserted into the Serpens cloud mosaic in the four IRAC bands.

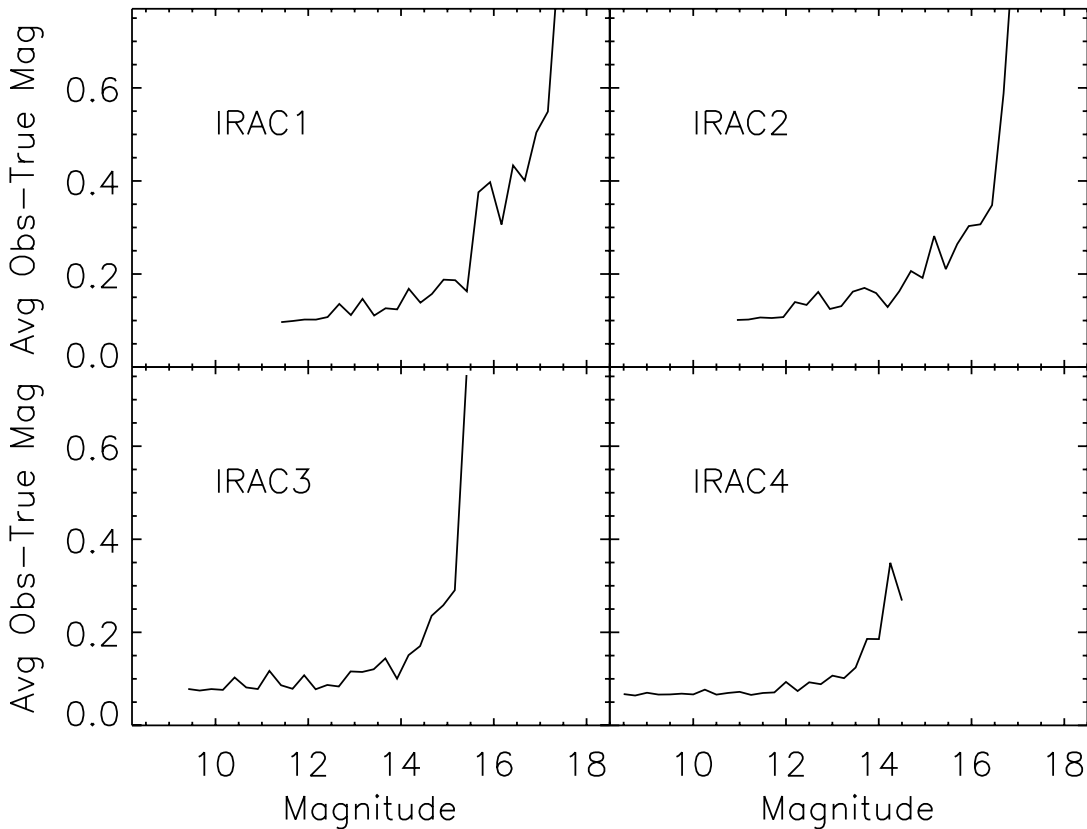


FIG. 7.—Plots of average error in the extracted magnitude for the artificial stars in the Serpens mosaic as a function of star magnitude for each band.

First, we have limited this most reliable subcatalog to include only sources that have greater than a 7σ detection. This criterion was applied to either all four IRAC bands for the statistical investigations that required four bands or, in the case of the 2MASS/IRAC color-color diagram described below, to the two shorter wavelength bands, 3.6 and $4.5\mu\text{m}$. In addition, it is somewhat problematic comparing photometry of objects extracted as “extended” to those for which a point-source profile was fitted for the photometry. Therefore, in all the discussion below, we have eliminated those sources that were extracted as extended. Table 3 shows that all these cuts result in a high-reliability catalog with a very small fraction of all the objects. Finally, there is clearly a small number of objects whose fluxes are saturated, even in the short, 0.4 s, exposure images taken in high dynamic range mode. Empirically we have determined that objects whose extracted magnitudes are brighter than 6.0 at $3.6\mu\text{m}$ or 5.0 at $4.5\mu\text{m}$ suffer from this problem in some cases. Therefore, we have also imposed this bright flux criterion to the final subcatalog used in the discussions that follow.

6. SOURCE STATISTICS

Table 3 lists the total number of sources extracted in each band for the Serpens cloud along with several subsets of the total. In addition, we show the numbers of sources in several trimmed subsets of the catalog that are used in subsequent discussions. In particular, the last two rows show the number of sources that are included in the color-color (or color-magnitude) diagrams, Figures 9, 10, and 11.

6.1. Background “Contamination”

There are two kinds of objects that contaminate our high-reliability catalog in terms of searching for members of the star-

forming groups in the Serpens dark cloud: background/foreground stars and extragalactic objects. These kinds of “contaminants” have very different characteristics from a large fraction of the youngest objects in the Serpens dark cloud.

We can address the question of background stellar contamination in two ways, both with our observations of the off-cloud areas and with theoretical models of the Galaxy’s stellar density. Figure 8 shows clearly that in terms of sheer numbers, most of the sources detected in this survey are background stars, since the number counts in the off-cloud regions are essentially the same as those in the Serpens cloud itself and both agree well with the model predictions in that direction in the Galaxy (see also Fig. 17). In the next section we discuss color-magnitude and color-color relationships for the on- and off-cloud regions and show that it is possible to pick out the contribution from the young stellar population relatively easily with these tools, at least those objects that have significant circumstellar dust emission.

The question of background galaxy contamination is different and more difficult in some ways. This is because the background galaxy number counts at the IRAC wavelengths have only become known with reasonable accuracy with the availability of *Spitzer* observations and because galaxies come in a much larger range of colors than do pure stellar photospheres. As for the background stellar contamination, we show in the following section that a large fraction of the background galaxy contamination in our sample can be removed by careful examination of color-magnitude and color-color diagrams. Of course, for both stars and galaxies, there are ranges of color and magnitude where only follow-up imaging and/or spectroscopy will enable a clear separation of young objects from background sources.

The data set that we have used to understand the galaxy component in our survey is the *Spitzer* Wide-Area Infrared Extragalactic

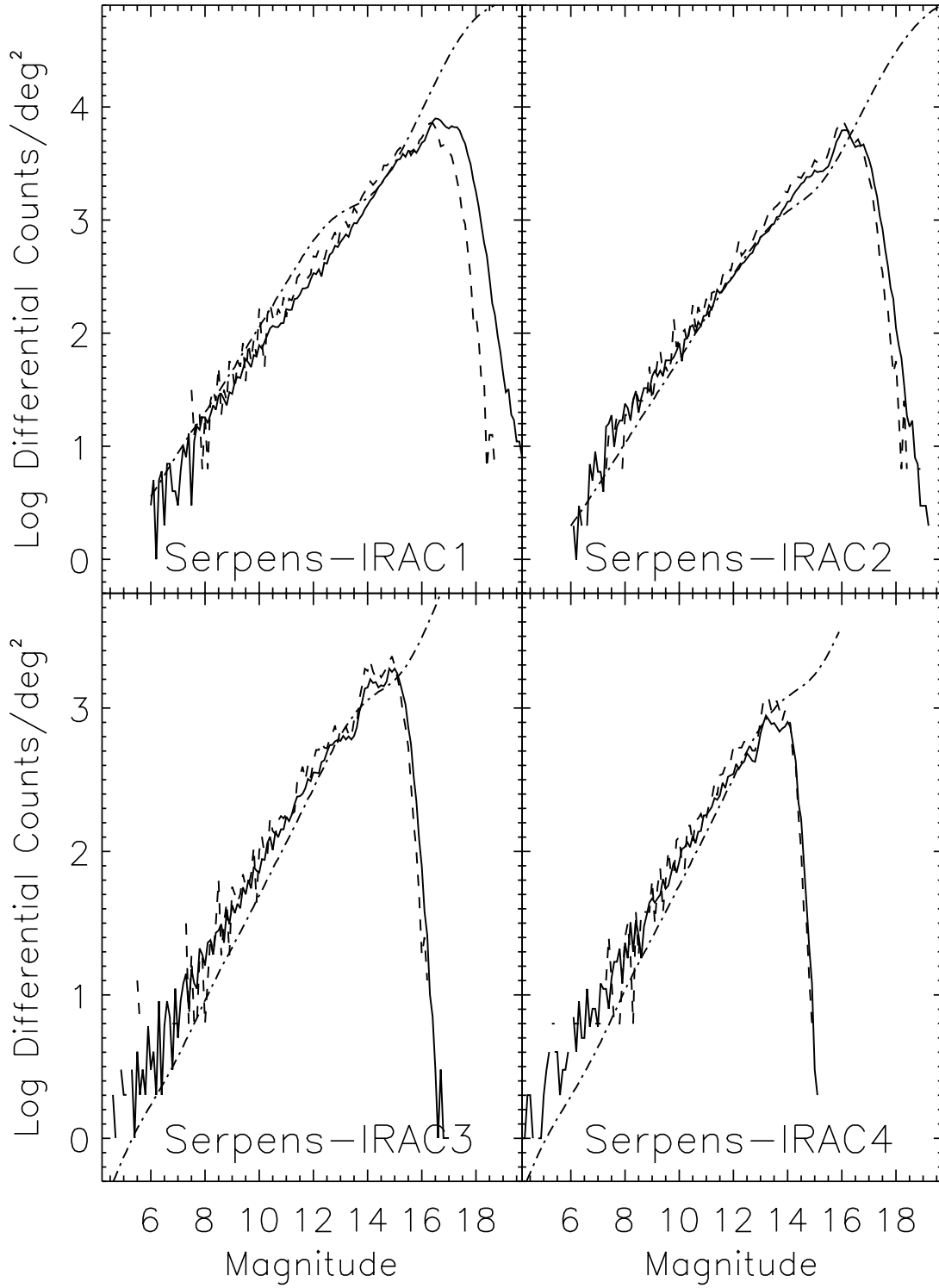


FIG. 8.—Differential source counts (solid line), off-cloud counts (dashed line, for the sum of off-cloud regions 1 and 6 normalized to 1 deg²), and predicted star counts (dash-dotted line) for extractions of all sources from the Serpens cloud data for the four IRAC bands.

Survey (SWIRE) Elais N1 data set (Surace et al. 2004). We have processed a portion of this survey completely through our c2d pipeline using the same processing parameters except for the depth of search, since the SWIRE sensitivity is about 1 mag fainter with its longer integration times. This processing produced a catalog of 103,557 sources, for a total area of 6.3 deg². In order to compare this catalog with our Serpens catalog we trimmed it in two ways. First, we simply extracted all the sources in the central

0.89 deg² to cover the same area as the Serpens map. In order to find a subset of SWIRE sources whose brightnesses would have been detected at the higher flux sensitivities of our c2d survey, we cut off the SWIRE catalog with a “completeness” function similar in shape to the completeness plots in Figure 5 but tuned to produce distributions whose faintest source was comparable in brightness to the faintest source in each band for the Serpens catalog. This resulted in a final, trimmed catalog of 591 sources

TABLE 3
NUMBERS OF SOURCES EXTRACTED IN SERPENS CLOUD

Source Category	3.6 μm	4.5 μm	5.8 μm	8.0 μm
Original Extractions				
Point sources.....	136800	111017	38224	18459
Extended sources.....	11028	2769	434	212
Assumed point sources ^a	51605	24421	3047	1065
Problem extractions ^b	9055	4574	1101	223
Total	208488	142781	42806	19959
S/N Cuts				
Number above 10 σ	170231	113073	25326	14435
Number above 15 σ	123388	77649	16591	10131
Bandmerged Catalog				
Final IRAC catalog objects	137785	107136	33320	16347
2MASS/IRAC catalog associations	25821	25822	21821	14661
IRAC1-2 ($>7 \sigma$)/2MASS point sources	13991
IRAC four-band point sources ($>7 \sigma$).....	13232

^a Too faint or too few image points to determine shape.

^b Nonconverging, too close to mosaic edge, too pointlike.

that is our best estimate of the catalog that would have been produced by observing the central square 0.89 deg^2 of the Elais N1 SWIRE region with the c2d integration time and the same criteria for inclusion into the final four-band high-quality detection set. (For the data in Fig. 11 the trimmed SWIRE catalog totaled 1942 sources, since only band 1 and 2 detections were required.)

6.2. Classification Based on Color and Magnitude

A large number of authors have shown that the simplest criterion for identifying young objects in star-forming regions is the presence of an “infrared excess.” Therefore, we have examined a number of color-color and color-magnitude distributions for the sources in our high-reliability catalog to determine which distribution shows most clearly a separation in characteristics of

objects that dominate in the control fields (off-cloud and SWIRE) versus a different population found only in the Serpens cloud data. We now discuss three of these distributions that seem to best delineate the young population in Serpens. Figure 9 shows a color-magnitude diagram for IRAC bands 2 and 4 for the Serpens cloud, the trimmed SWIRE catalog, and the off-cloud regions 1 and 6. Similarly, Figures 10 and 11 show color-color distributions for a pure IRAC color diagnostic, as well as a combination of IRAC bands 1 and 2 with H and K magnitudes from 2MASS. In all these plots, there is obviously a red population of objects that appears in the on-cloud data that is not present or at a much lower level in the off-cloud data.

Using these color and magnitude distributions as a guide, we have attempted to classify sources based on their spectral energy distributions (SEDs). This analysis takes place as part of the

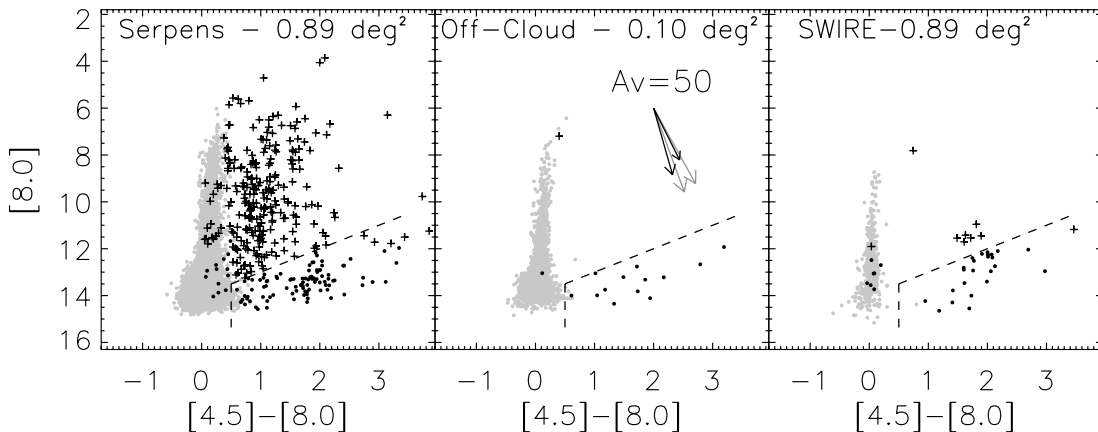


FIG. 9.—Color-magnitude diagram for (left) the Serpens cloud, (middle) off-cloud, and (right) trimmed SWIRE regions. The IRAC band 4 ($8.0 \mu\text{m}$) magnitude is plotted vs. the band 2 minus band 4 $[4.5] - [8.0]$ difference. The light gray points are objects identified as reddened stellar photospheres by fitting all available 2MASS and *Spitzer* data. The dark crosses are YSO candidates as described in the text, while the dark filled circles are all other identifications, most likely including a number of extragalactic objects. The dashed line shows the color-magnitude cut that defines the YSO candidate criterion in this color-magnitude space. The handful of objects bluer than the dashed line or fainter than it, which are marked by crosses, are YSO candidates chosen on the basis of MIPS data and will be discussed elsewhere. Several possible reddening vectors are shown, derived from deep near-infrared and *Spitzer* observations of dense cores by T. L. Huard et al. (2006, in preparation). The black vectors, appropriate for some of the densest regions found in cores, show the range of reddening possible for $R_V = 3.1$ and 5.5. The gray vectors are more appropriate for the moderate extinctions in the cloud.

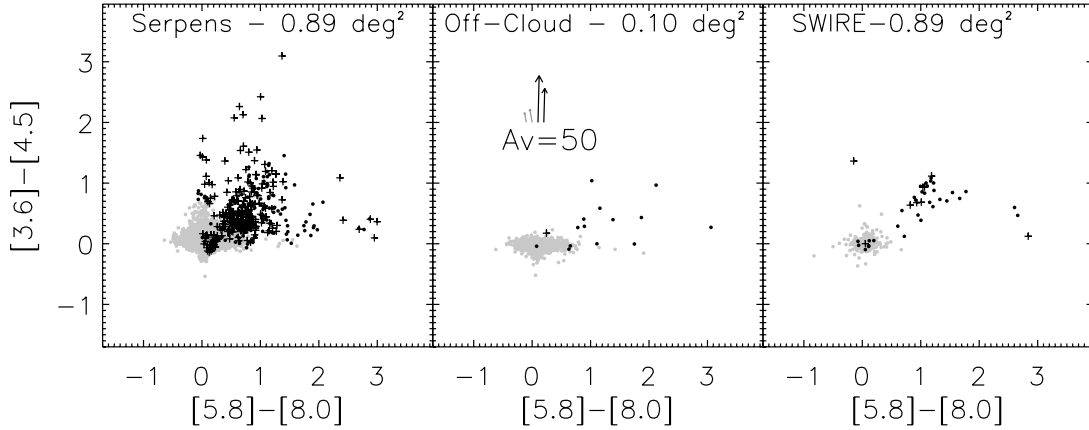


FIG. 10.—Color-color diagram, $[3.6] - [4.5]$ vs. $[5.8] - [8.0]$, for (left) the Serpens cloud, (middle) off-cloud, and (right) trimmed SWIRE regions. Symbols are the same as in Fig. 9.

bandmerging process described earlier. The two most important classification bins for the work discussed here are “star” and “young stellar object (YSO) candidate.” Objects classified as “star” have SEDs that can be well fitted by a reddened stellar photosphere for at least three bands, including the 2MASS data if available. The observed flux of a reddened star at a particular wavelength λ , F_{obs} , can be described by

$$\log \left[\frac{F_{\text{obs}}(\lambda)}{F_{\text{mod}}(\lambda)} \right] = \log K - 0.4C_{\text{ext}}(\lambda)A_V, \quad (1)$$

where F_{mod} is the stellar photosphere model, K is a scaling factor accounting for the distance to the star, and C_{ext} is the extinction at λ relative to visual extinction obtained from the dust extinction law. Therefore, K and A_V can be derived from the linear fit to this equation by adopting appropriate models for the stellar photosphere and dust extinction. The stellar photosphere models for the K-MIPS1 bands are adopted from the SSC’s “Star-Pet” tool,¹⁰ which is based on the Kurucz-Lejeune models. For the 2MASS bands, we translate the observed $J - H$ and $H - K$ colors of stars (Koornneef 1983) to fluxes relative to the K band and ignore the difference between the K and K_s bands. The dust extinction model is adopted from Weingartner

& Draine (2001) with $R_V = 5.5$. In addition, if a source has an SED that can be well fitted by a reddened photosphere with the exception of one band, we also classify it as “star.” This allowance for a discrepant flux accounts for the possibility of some problem with the photometry in one band or a prominent spectral line feature affecting a broadband flux.

YSO candidates are traditionally selected from sources with flux excess at near- to far-infrared wavelengths compared to the stellar photosphere. Unfortunately, many of the background galaxies also fit the same description. Because our observations are deep enough to have a nonnegligible amount of extragalactic sources, we attempt to identify the extragalactic “contamination” by using two statistical criteria derived from the SWIRE data, which is presumed to have essentially no Galactic star formation component.

The two statistical criteria we use for selecting YSO candidates are (1) $[4.5] - [8.0] > 0.5$ and (2) $[8.0] < 14 - ([4.5] - [8.0])$. The first criterion excludes the stellar component. Plotting the histogram of $[4.5] - [8.0]$ color for the SWIRE data, we find that there are two distinct components representing stellar and extragalactic sources with a local minimum between the two at $[4.5] - [8.0] \sim 0.5$ (see also Fig. 9). Although stars are already selected with the aforementioned SED fitting, this criterion also excludes peculiar stars with SEDs that cannot be fitted with our assumed photosphere models. For the extragalactic component

¹⁰ See <http://ssc.spitzer.caltech.edu/tools/starpet>.

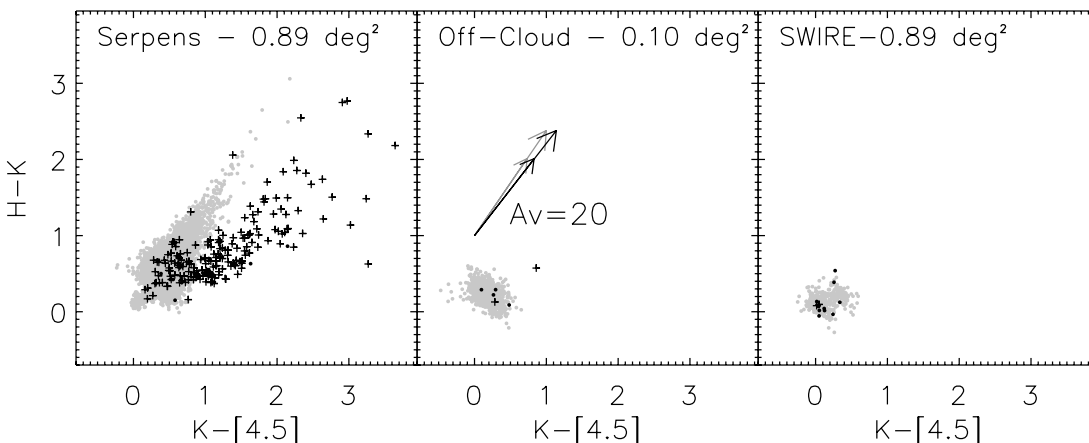


FIG. 11.—Color-color diagram, $H - K_s$ vs. $K_s - [4.5]$, for (left) the Serpens cloud, (middle) off-cloud, and (right) trimmed SWIRE regions. Symbols are the same as in Fig. 9.

of the SWIRE data, 95% of the sources lie under the diagonal line $[8.0] = 14 - ([4.5] - [8.0])$ of the $[8.0]$ versus $([4.5] - [8.0])$ color-magnitude diagram. Therefore, applying the second criterion excludes the majority of extragalactic sources in our data set. These criteria result in a list of 222 candidate YSOs. A small number (35) of additional YSO candidates have also been selected based on MIPS data with the same philosophy. The two statistical criteria used for the MIPS data are (1) $[24] - [8] > 0.7$ and (2) $[24] < 12 - ([24] - [8])$.

Although the identification as YSO candidate is based essentially on the $[4.5] - [8.0]$ color or longer wavelength data, Figures 10 and 11 show that the same objects generally occupy regions of those color-color diagrams that are nearly empty in the control region plots (off-cloud and SWIRE) with only a few exceptions. Thus, this classification appears to be well tuned to finding a population of objects associated with the Serpens cloud that have infrared excesses indicative of circumstellar material. We should point out that most of the population of objects in the SWIRE data set represented by crosses (YSO candidates) in all three figures are close to the magnitude cutoff for inclusion into the YSO candidate classification. If those objects in the SWIRE sample had been located behind the Serpens cloud, they would likely have been extincted and reddened below the cutoff in $[8.0]$ for YSO candidates.

There is one additional kind of contaminant that is likely to appear in our data at a relatively low level, asymptotic giant branch (AGB) stars. The *ISO* observations of, for example, van Loon et al. (1999) and Trams et al. (1999) show that the range of brightnesses of AGB stars in the LMC covers a span equivalent roughly to $8 < [8.0] < 12$, with colors generally equivalent to $[4.5] - [8.0] < 1$. For typical Galactic AGB stars, between 5 and 15 kpc from the Sun, this would imply $3 < [8.0] < 9$. The off-cloud fields (when normalized to the same area as the Serpens data) provide the best handle on the degree of contamination from AGB stars; we see one object classified as a YSO candidate in the off-cloud panel of Figure 9 with $[8.0] < 9$. Therefore, we expect the number of AGB stars contaminating the YSO candidate list in the Serpens cloud to be of the order of a half-dozen. As a further check, we have examined the entire set of off-cloud fields for such objects. In this combined area of 0.58 deg^2 , there are only three such YSO candidates. Finally, we have identified four AGB stars by their *Spitzer*-IRS spectra in the Serpens cloud (to be published elsewhere); all are brighter than our saturation cutoff of $[3.6] > 6 \text{ mag}$ and so do not even show up in our analysis.

The total number of objects classified as YSO candidates in the Serpens cloud is 257. Obviously from the color-color and color-magnitude diagrams a few of these are likely to be galaxies and/or AGB stars. On the other hand, as we discuss in § 9.2, a significant number of the faint red objects in Figure 9 (below the dashed line) may also be young substellar objects. Several authors have published estimates of *Spitzer* colors for pre-main-sequence objects at various evolutionary stages (Hartmann et al. 2005; Allen et al. 2004; Whitney et al. 2003). These estimates cover a wide range in infrared excess depending on evolutionary state and assumed model parameters. YSOs have been traditionally classified with Lada's Class I/II/III system (Lada 1987) according to the spectral index α at wavelengths greater than $2 \mu\text{m}$, or the more recent four-class system that inserts a "flat" category between Classes I and II (André & Montmerle 1994; Greene et al. 1994). The spectral index is

$$\alpha = \frac{d \log [\lambda F(\lambda)]}{d \log \lambda}, \quad (2)$$

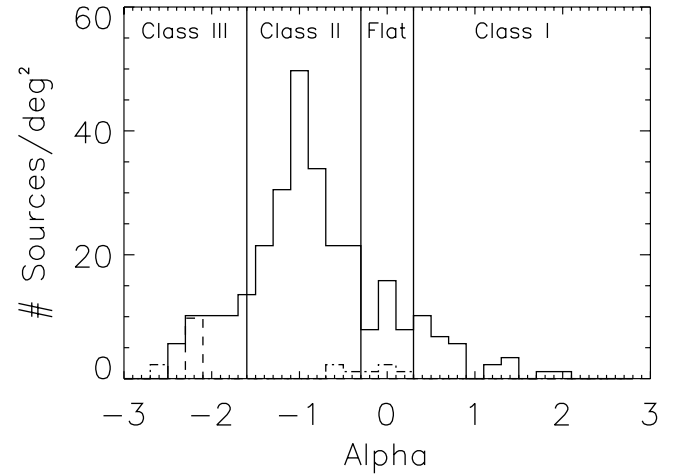


FIG. 12.—Histogram of the distribution of spectral slope, α , between 2 and $24 \mu\text{m}$ for the 257 candidate YSOs found from our *Spitzer* colors and magnitudes. The solid line shows the distribution for the Serpens cloud. For comparison, the dashed line shows the normalized distribution for the few objects found in the off-cloud region, and the dot-dashed line shows the same for the trimmed SWIRE catalog.

where λ is the wavelength and $F(\lambda)$ is the flux at that wavelength. Using the four-class system, for Class I sources, $0.3 \leq \alpha$; for "flat" sources, $-0.3 \leq \alpha < 0.3$; for Class II sources, $-1.6 \leq \alpha < -0.3$; for Class III sources, $\alpha < -1.6$.

We obtain α from a linear fit to the logarithm of the fluxes for all detections between the K_s band and the MIPS1 band with wavelength range $2-24 \mu\text{m}$. Note that because the expected value of α is ~ -2.8 for an average over stellar spectral types, we are not able to distinguish Class III objects from background stars. We find the numbers of Class I, flat, II, and III objects in our sample of candidate YSOs to be 30, 33, 163, and 31, respectively. Figure 12 shows the histogram of the distribution of α for the sample of YSO candidates.

7. COMPARISON WITH *IRAS* AND *ISO*

The most complete previous mid-infrared studies of the Serpens region have been made with *IRAS* (Zhang et al. 1988b) and *ISO* (Kaas et al. 2004), as well as the *IRAS* survey itself. So it is interesting to compare *Spitzer*'s view of Serpens with that from these previous space missions. The *IRAS* survey found 23 $12 \mu\text{m}$ sources within the area mapped in our survey. All of these can be identified with relatively bright $8 \mu\text{m}$ objects. The maps of Zhang et al. clearly show an extended emission region in the Serpens core (see also Zhang et al. 1988a), as well as compact sources associated with VV Ser and with the region they called Ser/G3–G6, i.e., our "cluster B." The *ISO* survey of Kaas et al. (2004) sampled a substantially smaller area roughly centered on the Serpens core but to much deeper mid-IR flux densities than did *IRAS*, typically $1 \sigma = 1 \text{ mJy}$ (for comparison, our *Spitzer* observations were made with $\sigma = 0.015 \text{ mJy}$ typically). Among the several hundred point sources detected, they identified 76 as having characteristics of YSOs, 20 Class I, 43 Class II, and 13 "flat-spectrum" sources. They found that the brightest Class I objects were strongly clustered in the core region (cluster A), while the Class II objects were more distributed, with typical cluster scales 2–5 times the 0.12 pc scale for the Class I's. We detected essentially all of their 44 YSO candidates that had $S/N > 5$, although in a few cases we classified them as reddened stars based on our data. We also detected roughly half of their lower S/N candidates.

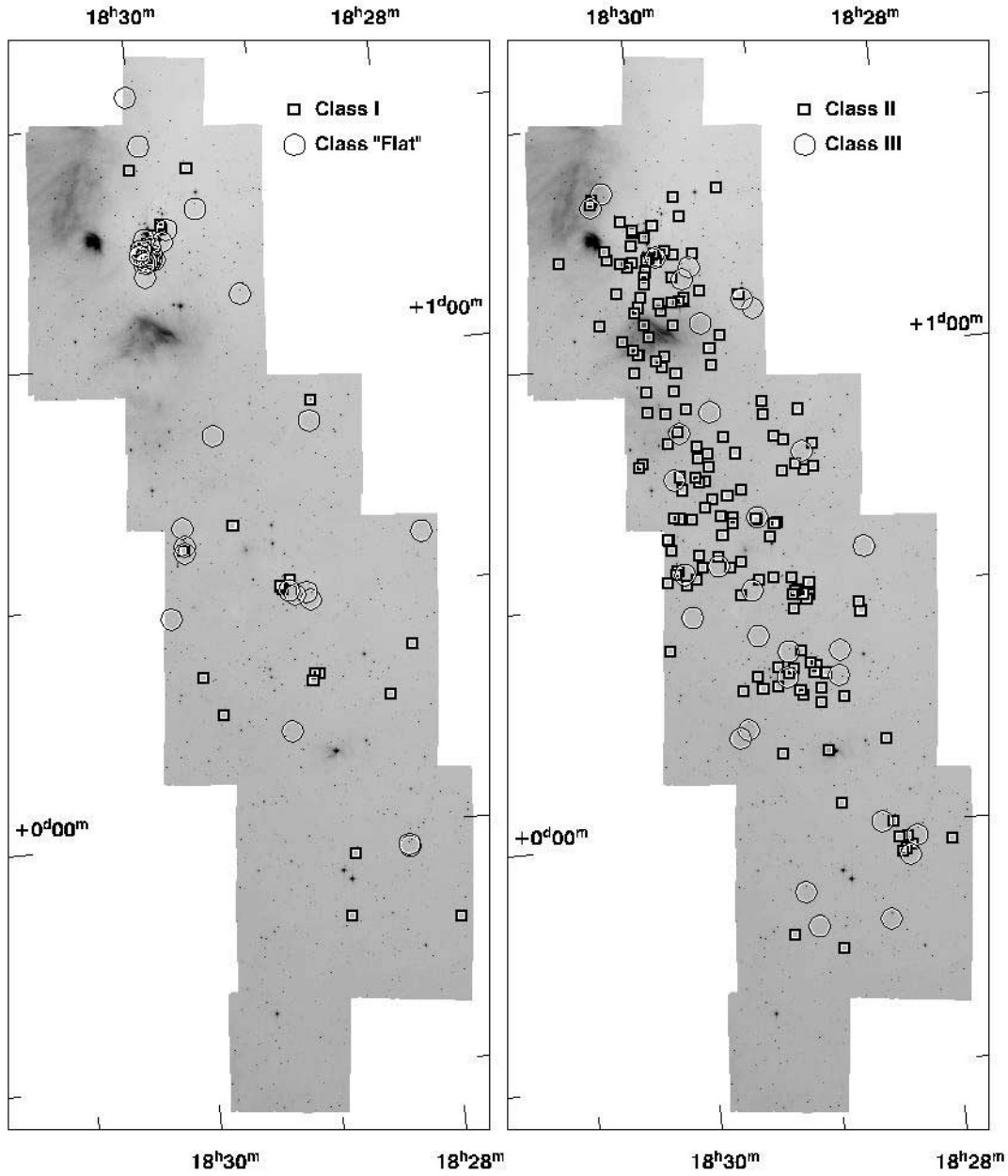


FIG. 13.—IRAC band 4 ($8.0 \mu\text{m}$) image with symbols drawn around sources identified as (left) Class I and flat and (right) Class II and III.

8. OVERALL CLOUD STRUCTURE AND SOURCE DISTRIBUTION

8.1. Clustering

Figure 13 shows the IRAC band 4 image with the positions of the nominal Class I, flat, Class II, and Class III objects selected above by their spectral slope, α . As was found by Kaas et al. (2004) at higher flux levels, there is an obvious clustering of Class I sources in the Serpens core region, cluster A. A second, less-dense cluster is found at the position we have called cluster B, with isolated individual sources in some other areas of the cloud. On the other hand, the Class II objects appear to be distributed much more widely and evenly around the mapped area. B. Merín et al. (2006, in preparation) discuss in much more detail the spatial distribution of objects with various levels of infrared excess and possible evolutionary implications. It is important to note, however, that an object that is intrinsically Class II may be

observed with Class I colors if it is located behind substantial extinction. Since the Class I objects are preferentially located in areas of higher extinction, it is possible that some of these are, in fact, misclassified Class II sources. Obviously, this effect can also apply to objects near other class boundaries as well.

8.2. Extinction

There are several tracers of column density that can be used to study the spatial distribution of gas and dust in the cloud. Each tracer has advantages and limitations, but the technique using color excesses of background stars provides a reasonably reliable measure of column density. Figure 14 shows the $4.5 \mu\text{m}$ mosaic overlaid with extinction contours constructed using the near-infrared color excess (NICE) method (e.g., Lada et al. 1999; Huard et al. 2006), making use of 2MASS sources, and convolving the line-of-sight extinctions with a Gaussian beam with FWHM of $5'$. Compared to star-counting methods, which

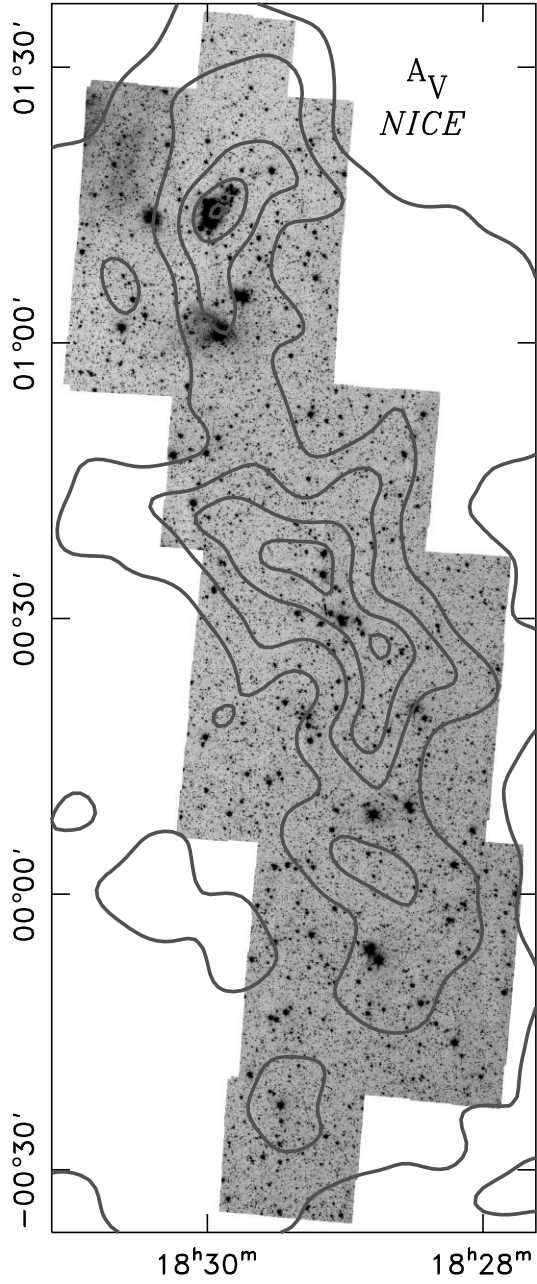


FIG. 14.—Contours of extinction overlaid on the $4.5 \mu\text{m}$ mosaic. The contours represent 5' beam-averaged extinction at $A_V = [2, 4, 6, 8, 10]$ mag, derived using 2MASS observations of background stars and the NICE method (see § 8.2).

reliably trace the large-scale structure, the NICE method provides a greater dynamic range and angular resolution, especially in regions of moderate extinction. Similar to Enoch et al. (2006), we eliminate from the 2MASS catalog most foreground and embedded sources that would yield unreliable extinction estimates when constructing the extinction map. In order to calibrate the extinction map, we identified an off-cloud region that was free of structure and assumed to be a nonextincted region near the Serpens cloud. This off-cloud region, centered on $(18^h28^m, +02^\circ21' [\text{J}2000.0])$, was a 1.0×0.25 field containing more than 7400 stars from which we derived a mean intrinsic $H - K$ color for the background stellar population of 0.238 ± 0.002 mag.

We see from Figure 14 that our mosaic of the Serpens cloud is almost entirely within the $A_V = 2$ mag contour, and more than

half of the mosaic covers extinctions of $A_V > 4$ mag. Comparing Figure 4 with the extinction contours in Figure 14, we see that the extinction peaks in regions of the Serpens cloud identified as cluster A and cluster B, the same regions exhibiting the highest density of Class I sources. While the apparent extinction in these regions is seen to reach $A_V \approx 10$ mag, the peak extinctions are likely greater. Our map relies on the detection of background stars at all of J , H , and K_s by 2MASS. Particularly in dense regions with moderate extinctions, $A_V > 8-10$ mag, on angular scales comparable to the beam size (e.g., 5' in this case), the extinctions derived from 2MASS observations using the NICE method tend to be underestimates. Typically, lines of sight toward background stars that are detected at all of the near-infrared bands by 2MASS underrepresent the densest regions of the cloud.

8.3. Diffuse Extended Emission

Figure 4 provides the most beautiful and clearest view of the range of diffuse dust and gas emission shortward of $10 \mu\text{m}$. The most obvious diffuse features in this figure are large areas of red emission in cluster A, together with smaller areas in cluster B and around the Herbig Ae star VV Ser. The emission around VV Ser is the subject of a detailed study and modeling effort by K. M. Pontoppidan et al. (2006a, in preparation; 2006b, in preparation), so we do not discuss it further here. Since band 4 of IRAC, $8.0 \mu\text{m}$, is nearly coincident with strong polycyclic aromatic hydrocarbon (PAH) emission bands, the simplest and most likely explanation for all of the diffuse red emission in this figure is that it represents PAH (and other dust) grains excited by a diffuse UV field. Indeed, this is the clear result for at least the diffuse $8 \mu\text{m}$ emission around VV Ser in the studies of Pontoppidan et al.

8.4. Shock-excited Gas

The second obvious kind of features in Figure 4 are small areas of green diffuse emission, especially in the two clusters, A and B. These are likely to be examples of a well-studied phenomenon in other regions of star formation, regions of shock-excited gas, probably associated with YSOs with outflows (e.g., Noreiga-Crespo et al. 2004). Smith & Rosen (2005) have modeled this as emission from a combination of molecular hydrogen lines. Several previous optical and near-infrared studies have identified a variety of outflow shocks in the core (Ziener & Eisloffel 1999; Hodapp 1999; Herbst et al. 1997; Huard et al. 1997), at least some of which can be identified in our $4.5 \mu\text{m}$ image. It is beyond the scope of this paper, however, to discuss the issue of which area of strong green (IRAC band 2) emission is an individual outflow, and which point source is likely to be the exciting source for each outflow. Joint optical and near-infrared line studies, together with these *Spitzer* data, will be the best way to resolve these questions.

9. SELECTED SOURCES

9.1. Cluster B

One of the most striking regions, not previously recognized as a dense center of star formation in the Serpens cloud, is the area noted in Figure 4 as cluster B. Although four optical emission line sources had previously been noted here (Cohen & Kuhi 1979; see also the Herbig & Bell catalog; Herbig & Bell 1988), as well as two *IRAS* sources, our *Spitzer* maps show that there is a dense collection of red sources here. Indeed, as noted above, this cluster has the second highest density of Class I sources in the region. Figure 4 also shows, as mentioned above, that there are probably several outflows in this region producing extended

TABLE 4
YSO CANDIDATES IN CLUSTER B

Source ID	Name/Position (SSTc2d)	α	3.6 μm Flux (mJy)	4.5 μm Flux (mJy)	5.8 μm Flux (mJy)	8.0 μm Flux (mJy)	24.0 μm Flux (mJy)
1.....	J182852.56+003053.9	-0.39	2.88 ± 0.35	3.43 ± 0.41	3.18 ± 0.38	1.94 ± 0.23	...
2.....	J182852.72+002923.2	-1.13	0.37 ± 0.04	0.59 ± 0.07	0.56 ± 0.07	0.36 ± 0.04	...
3.....	J182852.77+002846.5	0.15	1.93 ± 0.23	2.61 ± 0.31	2.56 ± 0.31	3.29 ± 0.39	16.2 ± 2.4
4.....	J182854.47+002947.4	0.15	5.97 ± 0.72	19.100 ± 2.29	28.90 ± 3.47	15.80 ± 1.9	...
5.....	J182854.51+002852.2	-0.84	17.4 ± 1.9	37.9 ± 4.6	45.5 ± 5.5	24.8 ± 3.0	5.08 ± 0.76
6.....	J182856.02+002933.4	-0.57	0.91 ± 0.11	2.10 ± 0.25	2.36 ± 0.28	1.37 ± 0.16	...
7.....	J182858.66+003009.3	-1.04	0.57 ± 0.07	1.03 ± 0.12	1.02 ± 0.12	0.59 ± 0.07	...
8.....	J182859.47+003002.8	-0.58	38.6 ± 4.6	43.7 ± 5.2	45.2 ± 5.4	48.1 ± 5.8	84.9 ± 12.7
9.....	J182900.19+002936.4	-0.15	1.44 ± 0.17	1.70 ± 0.20	2.17 ± 0.26	2.61 ± 0.31	...
10.....	J182900.83+002746.7	-0.37	9.55 ± 1.2	10.4 ± 1.3	10.3 ± 1.2	12.1 ± 1.5	29.8 ± 4.5
11.....	J182901.08+003145.1	-0.78	64.5 ± 7.7	79.4 ± 9.5	75.6 ± 9.1	72.7 ± 8.7	74.7 ± 11
12.....	J182901.22+002933.0	-0.52	92.8 ± 11	98.7 ± 12	95.5 ± 11	96.5 ± 12	...
13.....	J182902.12+003120.5	0.50	1.28 ± 0.15	1.70 ± 0.20	1.53 ± 0.18	1.01 ± 0.12	22.9 ± 3.4
14.....	J182902.84+003009.4	-0.18	16.5 ± 2.0	19.5 ± 2.3	22.4 ± 2.7	28.0 ± 3.4	93.6 ± 14
15.....	J182905.58+003015.7	0.69	0.29 ± 0.03	0.54 ± 0.06	0.88 ± 0.11	1.12 ± 0.13	...
16.....	J182906.19+003043.2	1.50	8.63 ± 1.0	52.0 ± 6.2	99.1 ± 11.9	135 ± 16	1850 ± 280
17.....	J182906.76+003034.2	1.87	3.23 ± 0.39	14.0 ± 1.7	16.3 ± 2.0	22.7 ± 2.7	1130 ± 170
18.....	J182907.09+003043.1	1.37	0.49 ± 0.06	2.54 ± 0.30	3.83 ± 0.46	3.74 ± 0.45	...
19.....	J182909.83+003155.8	-1.42	1.45 ± 0.17	1.87 ± 0.22	1.73 ± 0.21	1.07 ± 0.13	...
20.....	J182916.86+003146.4	-0.78	0.95 ± 0.11	0.76 ± 0.09	0.47 ± 0.06	0.53 ± 0.06	1.77 ± 0.27
21.....	J182920.95+003034.5	-1.71	928 ± 110	572 ± 69	572 ± 69	356 ± 43	205 ± 31
22.....	J182924.88+003408.3	-0.66	1.67 ± 0.20	2.06 ± 0.25	2.24 ± 0.27	2.12 ± 0.25	2.30 ± 0.34
23.....	J182926.41+003004.3	-0.73	4.59 ± 0.55	4.09 ± 0.49	3.50 ± 0.42	3.78 ± 0.45	9.18 ± 1.4
24.....	J182930.56+003337.6	-0.61	3.16 ± 0.38	2.86 ± 0.34	2.51 ± 0.30	3.03 ± 0.36	7.04 ± 1.06

4.5 μm emission. A detailed analysis of the properties of these objects will be presented in a forthcoming paper where we also will include the longer wavelength results from the *Spitzer* MIPS instrument. We list the positions, spectral slopes (α), and measured IRAC flux (and MIPS 24 μm from W. Spiesman et al. 2006, in preparation) densities for a number of the objects in Table 4 from a 12' \times 12' area and show some of their energy distributions in Figure 15.

9.2. The Lowest Luminosity Objects

One of the major strengths of the *Spitzer Space Telescope* is its sensitivity to very low luminosity objects. A detailed analysis of the implications of our deep IRAC mapping for understanding the lowest luminosity young “stars” will be discussed in a future paper. We have, however, conducted a preliminary analysis of the young substellar content of the Serpens dark cloud based on the statistics of the high-quality subsamples discussed above. The faintest objects in our sample clearly include some number of extragalactic objects, so without follow-up observations it will be difficult to determine which of the faint sample is a Galactic source. However, we can determine statistically the relative contributions to the faintest objects from very low luminosity cloud members and distant background objects by a careful comparison of the Serpens cloud data with our off-cloud data and SWIRE sample. The most reliable comparison should be with the off-cloud sample, since it was obtained with exactly the same observing parameters and viewed the general Galactic stellar population (and background extragalactic population) in essentially the same direction as the on-cloud data. The only significant difference is that by choice the off-cloud sample has less extinction on average than does the Serpens cloud sample. Thus, a fairly conservative approach should be to subtract the off-cloud surface density at any given magnitude from the on-cloud numbers, since the off-cloud numbers should be slightly higher than they would have been if viewed through the same

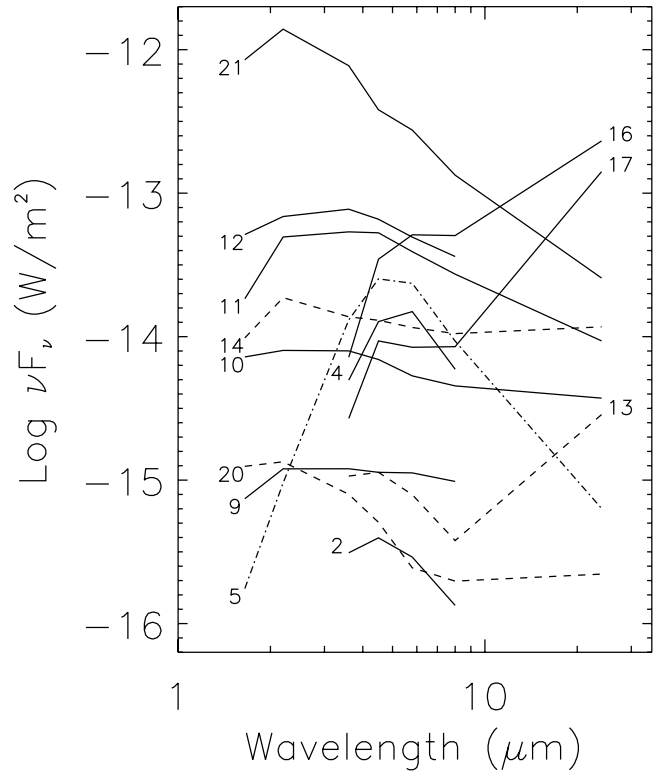


FIG. 15.—Energy distributions of a selection of YSO candidates from the list in Table 4. The curves are labeled by the source ID number in Table 4.

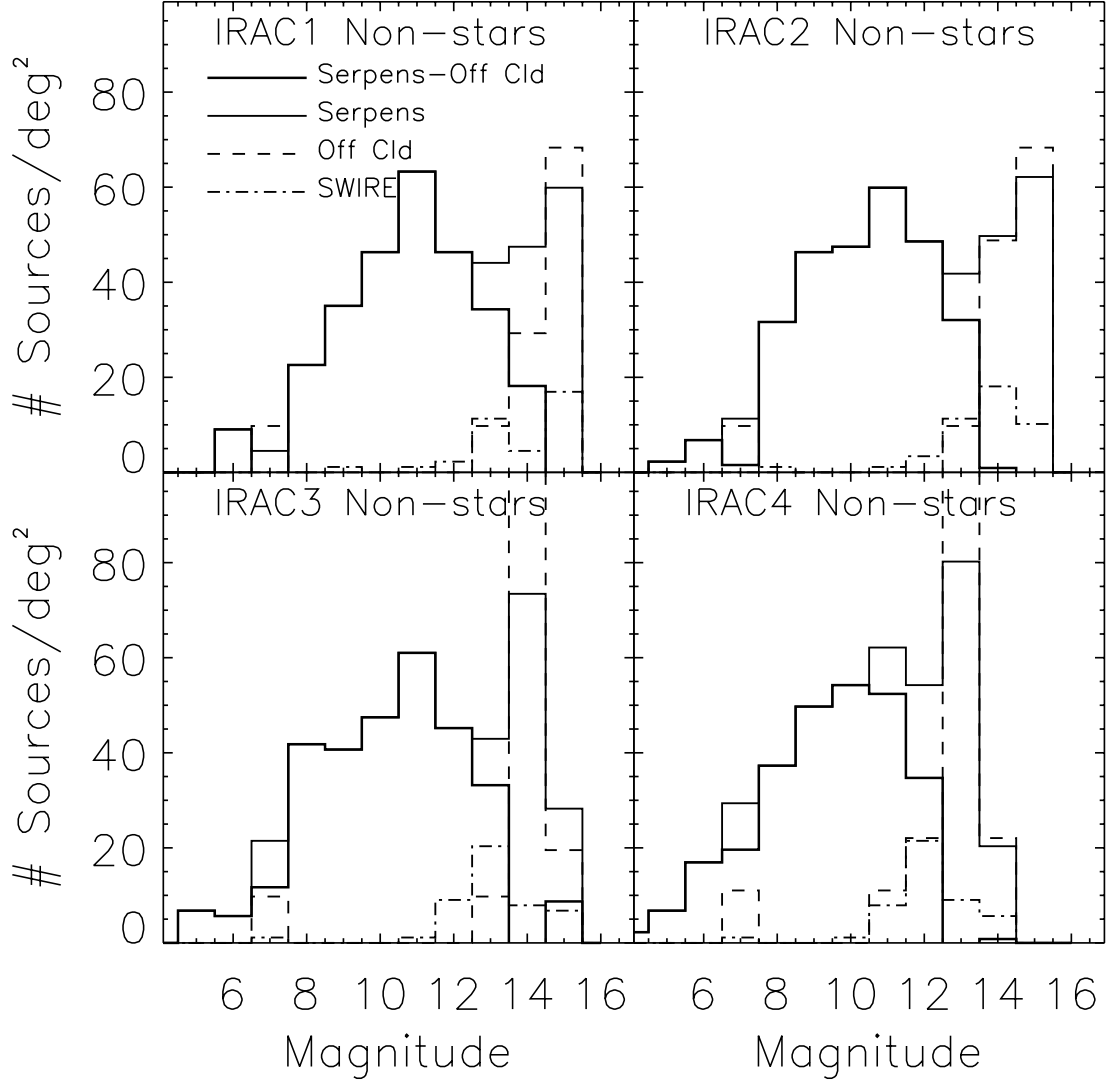


FIG. 16.—Histograms of source counts vs. magnitude for objects that were redder than reddened background stars for each IRAC band. In each panel the heavy solid line shows the difference between the on-cloud counts and the off-cloud counts normalized to the same area (1 deg^2). The light solid line is the on-cloud counts; the dashed line is the normalized off-cloud counts; and the dot-dashed line is the histogram for the trimmed SWIRE catalog.

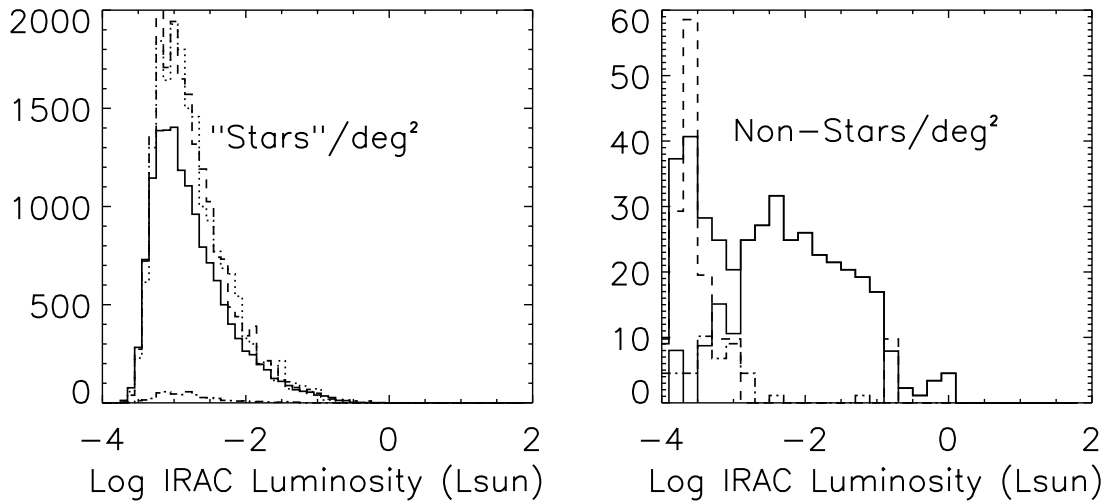


FIG. 17.—Histograms of the IRAC (3–10 μm) luminosity assuming a distance to all the objects equal to the adopted distance to the Serpens cloud of 260 pc. The lines have the same meaning as in Fig. 16. In the left panel the dotted line shows, in addition, the counts of objects identified as reddened stellar photospheres for the lowest extinction region of the Serpens cloud, illustrating that the off-cloud and on-cloud counts are essentially identical in regions of comparable extinction.

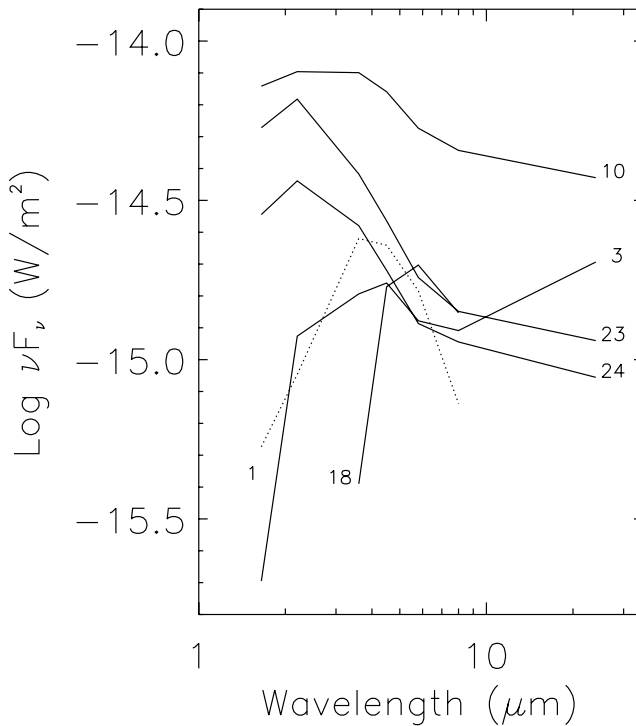


FIG. 18.—Energy distributions of a selection of low-luminosity YSO candidates from the list in Table 4. The curves are labeled by the source ID number in the table.

extinction as the typical regions in the Serpens cloud. Furthermore, since the lifetime of infrared excesses around very low mass objects may be quite long, it is possible that some fraction of the infrared excess sources in the off-cloud region are young substellar objects that have moved away from the densest parts of the Serpens cloud. Note, for example, that the background galaxy counts expected from the SWIRE observations trimmed to the c2d limits are well below the off-cloud counts in Figures 9, 10, and 11.

Figures 16 and 17 show two different ways to display the population of candidate YSOs as a function of brightness. Figure 17 (*left*) shows that the off-cloud counts for objects identified as reddened stellar photospheres are about 30% higher than the on-cloud counts for the objects close to our detection limit. This is almost certainly due to the much lower average extinction in the off-cloud areas. In particular, the dotted curve in Figure 17 (*left*) shows the on-cloud star counts for two small regions totaling 0.07 deg^2 at the north and south end of the mapped region where the extinction is at a minimum. The fact that this distribution is essentially identical to the off-cloud distribution demonstrates that the counts for *any* class of object within the denser parts of the Serpens cloud will be lower than in the off-cloud region due to extinction, even at IRAC wavelengths.

In Figure 17 (*right*) and in the four panels of Figure 16 the thick line shows that when the off-cloud counts (per deg^2) are

subtracted from the on-cloud counts (*thick line*), there is a residual population of objects with infrared excess down to the detection limits of our observations. This is true even though we have made no correction for the higher extinction to the average source in the Serpens cloud relative to the off-cloud field. Figure 17 (*left*) suggests that it may be appropriate to correct downward the off-cloud counts of “nonstars” at the lower luminosities by a factor of the order of 1.3, which would imply even more lower luminosity infrared-excess objects in Serpens that are likely to be young cloud members.

Although it is impossible to be sure which of the infrared-excess objects in these plots is a young substar, Figure 17 suggests that above a $3\text{--}10 \mu\text{m}$ luminosity of $10^{-3} L_\odot$ most of the infrared-excess objects are likely to be young objects within the Serpens cloud. Figure 18 shows the energy distributions of the five such objects that are located within cluster B. We have included the MIPS 24 μm photometry from a companion study by W. Spiesman et al. (2006, *in preparation*) where available. Without very sensitive follow-up spectroscopy, it is impossible to be sure that these are not background galaxies, for example. But statistically, Figure 17 suggests that very few are.

10. SUMMARY

We have identified more than 250 likely young objects embedded in the Serpens dark cloud, a factor of 3 more than the most sensitive previous survey by Kaas et al. (2004) with *ISO*. A wide variety of energy distributions is observed for sources whose colors imply infrared excesses longward of $3 \mu\text{m}$. A particularly rich area of star (and substellar) formation is located about 1° southwest of the well-studied Serpens core. This region, cluster B, includes a number of Class I sources and several likely outflows. Estimates of background confusion by stars and extragalactic objects suggest that there is a population of infrared-excess sources in the Serpens cloud down to the lowest reliable luminosities in our survey, $L_{3\text{--}10 \mu\text{m}} \sim 10^{-3} L_\odot$, and possibly lower. Deeper imaging observations, as well as follow-up spectroscopy, will be important to determine this limit and the nature of the objects at these low luminosities.

Support for this work, part of the *Spitzer* Legacy Science Program, was provided by NASA through contracts 1224608, 1230782, and 1230779 issued by the Jet Propulsion Laboratory, California Institute of Technology, under NASA contract 1407. K. E. Y. was supported by NASA under grant NGT5-50401 issued through the Office of Space Science. Astrochemistry in Leiden is supported by a NWO Spinoza grant and a NOVA grant. J. K. J. was supported by NASA Origins grant NAG5-13050. This publication makes use of data products from the Two Micron All Sky Survey, which is a joint project of the University of Massachusetts and the Infrared Processing and Analysis Center/California Institute of Technology, funded by NASA and the National Science Foundation. We also acknowledge use of the SIMBAD database.

REFERENCES

- Allen, L. E., et al. 2004, *ApJS*, 154, 363
- André, P., & Montmerle, T. 1994, *ApJ*, 420, 837
- Berrilli, F., Corciulo, G., Ingrosso, G., Lorenzetti, D., Nisini, B., & Strafella, F. 1992, *ApJ*, 398, 254
- Blake, G. A., & Boogert, A. C. A. 2004, *ApJ*, 606, L73
- Cambrésy, L. 1999, *A&A*, 345, 965
- Chavarria-K., C., de Lara, E., Finkenzeller, U., Mendoza, E. E., & Ocegueda, J. 1988, *A&A*, 197, 151
- Cohen, M., & Kuhi, L. V. 1979, *ApJS*, 41, 743
- Eiroa, C., & Casali, M. M. 1992, *A&A*, 262, 468
- Enoch, M. L., et al. 2006, *ApJ*, 638, 293
- Evans, N. J., II, Mundy, L. G., Harvey, P. M., Huard, T., Brooke, T. Y., Koerner, D. W., & Dunham, M. 2005, Second Delivery of Data from the c2d Legacy Project: IRAC and MIPS (Pasadena: Caltech), http://data.spitzer.caltech.edu/popular/c2d/20050705_enhanced_v1/Documents/
- Evans, N. J., II, et al. 2003, *PASP*, 115, 965

- Greene, T. P., Wilking, B. A., André, P., Young, E. T., & Lada, C. J. 1994, ApJ, 434, 614
- Hartmann, L., et al. 2005, ApJ, 629, 881
- Harvey, P. M., Wilking, B. A., & Joy, M. 1984, ApJ, 278, 156
- Herbig, G. H., & Bell, K. R. 1988, Third Catalog of Emission-Line Stars of the Orion Population (Santa Cruz: Lick Obs.), <http://www-int.stsci.edu/~welty/HBC/HBCintro.html>
- Herbst, T. M., Beckwith, S. V. W., & Robberto, M. 1997, ApJ, 486, L59
- Hillenbrand, L. A., Strom, S. E., Vrba, F. J., & Keene, J. 1992, ApJ, 397, 613
- Hodapp, K. W. 1999, AJ, 118, 1338
- Hogerheijde, M. R., van Dishoeck, E. F., & Salverda, J. M. 1999, ApJ, 513, 350
- Huard, T. L., Weintraub, D. A., & Kastner, J. H. 1997, MNRAS, 290, 598
- Huard, T. L., et al. 2006, ApJ, 640, 391
- Hurt, R. L., & Barsony, M. 1996, ApJ, 460, L45
- Kaas, A. A., et al. 2004, A&A, 421, 623
- Koornneef, J. 1983, A&A, 128, 84
- Lada, C. J. 1987, in IAU Symp. 115, Star Forming Regions, ed. M. Peimbert & J. Jugaku (Dordrecht: Reidel), 1
- Lada, C. J., Alves, J., & Lada, E. A. 1999, in The Physics and Chemistry of the Interstellar Medium, ed. V. Ossenkopf, J. Stutzki, & G. Winnewisser (Herdecke: GCA), 161
- Li, W., Evans, N. J., II, Harvey, P. M., & Colomé, C. 1994, ApJ, 433, 199
- Makovoz, D., & Marleau, F. R. 2005, PASP, 117, 1113
- Noreiga-Crespo, A., et al. 2004, ApJS, 154, 352
- Press, W. H., Teukolsky, S. A., Vetterling, W. T., & Flannery, B. P. 1992, Numerical Recipes in C (Cambridge: Cambridge Univ. Press)
- Schechter, P. L., Mateo, M., & Saha, A. 1993, PASP, 105, 1342
- Sivia, D. S. 1996, A Bayesian Tutorial (Oxford: Clarendon)
- Smith, M. D., & Rosen, R. 2005, MNRAS, 357, 1370
- Straizys, V., Cernis, K., & Bartasiute, S. 1996, Baltic Astron., 5, 125
- Surace, J. A., et al. 2004, The SWIRE ELAIS N1 Image Atlases and Source Catalogs (Pasadena: Spitzer Science Center), <http://ssc.spitzer.caltech.edu/legacy/>
- Testi, L., & Sargent, A. L. 1998, ApJ, 508, L91
- Testi, L., Sargent, A. L., Olmi, L., & Onello, J. S. 2000, ApJ, 540, L53
- Trams, N. R., et al. 1999, A&A, 346, 843
- van Loon, J. Th., et al. 1999, A&A, 351, 559
- Wainscoat, R. J., et al. 1992, ApJS, 83, 111
- Weingartner, J. C., & Draine, B. T. 2001, ApJ, 548, 296
- Whitney, B. A., Wood, K., Bjorkman, J. E., & Cohen, M. 2003, ApJ, 598, 1079
- Winston, E., et al. 2005, in Protostars and Planets V, ed. V. Mannings et al. (Houston: LPI), 8182
- Zhang, C. Y., Laureijs, R. J., & Clark, F. O. 1988a, A&A, 196, 236
- Zhang, C. Y., et al. 1988b, A&A, 199, 170
- Ziener, R., & Eisloffel, J. 1999, A&A, 347, 565